energies

MDPI

Article

Performance Analysis of High-Speed Electric Machines Supplied by PWM Inverters Based on the Harmonic Modeling Method

Marko Merdžan

Electromechanics and Power Electronics Group, Department of Electrical Engineering, Eindhoven University of Technology, P.O. Box 513, 5600 MB Eindhoven, The Netherlands; M.Merdzan@tue.nl

Abstract: This paper presents a method for the performance analysis of high-speed electric machines supplied with pulse-width modulated voltage source inverters by utilizing a fast analytical model. By applying a strict mathematical procedure, effective expressions for the calculation of rotor eddy current losses and electromagnetic torque are derived. Results obtained by the approach suggested in this study are verified by the finite element model, and it is shown that the proposed method is superior in comparison to the finite element method in terms of computation time. The proposed method enables fast parameter variation analysis, which is demonstrated by changing the inverter switching frequency and electric conductivity of the rotor and analyzing the effects of these changes on rotor eddy current losses. The presented work separately models effects of the permanent magnet and pulse-width modulated stator currents, making it suitable for the analysis of both high-speed permanent magnet machines and high-speed induction machines.

Keywords: high-speed machines; pulse width modulation; eddy current losses; electromagnetic torque; harmonic modeling; finite element modeling; voltage source inverters; permanent magnet machines; solid rotor induction machines; electrically assisted turbochargers

check for updates

Citation: Merdžan, M. Performance Analysis of High-Speed Electric Machines Supplied by PWM Inverters Based on the Harmonic Modeling Method. *Energies* **2021**, *14*, 2606. https://doi.org/10.3390/en14092606

Academic Editors: Yacine Amara and Andrea Mariscotti

Received: 20 February 2021
Accepted: 23 April 2021
Published: 2 May 2021

Publisher's Note: MDPI stays neutral with regard to jurisdictional claims in published maps and institutional affiliations.

Copyright: © 2021 by the author. Licensee MDPI, Basel, Switzerland. This article is an open access article distributed under the terms and conditions of the Creative Commons Attribution (CC BY) license (https://creativecommons.org/licenses/by/4.0/).

1. Introduction

In modern times, the use of electric machines in automotive applications increases continuously. Current tendencies in this field mainly assume the development of fully electric and hybrid vehicles, where propulsion is done solely or partly by electric machines [1–4]. Electric machines in vehicles are also widely used in different auxiliary systems, such as transmission oil pumps [5] and cooling fan systems [6]. They can also be found in electrically assisted turbochargers [7]. Here, a very high-speed (above 100,000 RPM) electric machine is used to drive a compressor independently of the engine, eliminating turbo lag and improving the overall performance [8]. When there is enough power supplied from the exhaust to the turbine inlet, the machine can work in the generator mode [9], reusing some energy contained in the exhaust heat.

High-speed permanent magnet (PM) machines are widely used for turbochargers as they provide high power density imposed by the limited machine volume. A significant setback associated with high power density is the high loss density. In a high-temperature environment, where heat removal from the rotor is very difficult, high loss density increases the risk of demagnetization. Furthermore, high-speed machines are driven by power electronics converters that inject non-sinusoidal currents in stator windings. Distorted current waveforms cause eddy current losses in the rotor, further increasing the risk of overheating and demagnetization which can result in a serious fail.

To properly predict the performance of a machine supplied with non-sinusoidal currents, a thorough modeling approach that takes into account all significant effects has to be applied during the design process. Although finite element method (FEM) is used by some authors [10–12], for high-speed machines supplied with pulse-width modulated

(PWM) currents, this method is very time consuming, which limits possibilities to perform effective parameter variation analysis. Namely, the accuracy of transient FEM simulations is very sensitive to the size of the simulation step, which has to be chosen according to the highest frequency in the spectrum of stator currents. In the case of PWM currents, harmonic components appear at frequencies that are an order of magnitude (and more) higher than the fundamental frequency. This requires a small simulation step and results in a very long computation time.

As alternatives to transient FEM, analytical methods are preferred, since they require shorter computation time and allow fast parameter optimization. A widely used analytical technique for the modeling of electric machines is the magnetic equivalent circuits (MEC) method [13,14]. It requires that the magnetic flux lines are known in advance. Therefore, it is not easily applicable when PWM currents are present in stator windings, as it is difficult to predict the exact spatial distribution of PWM caused eddy currents in the rotor. Consequently, when MEC is used to model eddy currents, it typically does not include the effect of the eddy current reaction field [15,16]. In high-speed applications, this can significantly overestimate the field and consequently eddy current losses. Furthermore, the accuracy of MEC is determined by the size of individual MEC elements, similarly to the accuracy of FEM which depends on the quality of the mesh.

A very effective method for the analysis of eddy current-related problems in electric machines is the harmonic modeling (HM) method. It is based on Fourier analysis of spatial harmonics in the circumferential direction of the machine and it has been proven as a suitable tool for the analysis of the electromagnetic field in high-speed machines [17,18]. It is a mesh-free method that easily accounts for the reaction field of eddy currents and allows multiple time harmonics in stator currents. However, the available literature on this method rarely treats PWM supply specifically and in sufficient detail. Peculiarities associated with PWM modulation are mostly not considered and time harmonics in stator currents are usually modeled in a manner that does not reflect realistic PWM currents. In [19], PWM caused current ripple is represented by a single sinusoidal waveform at switching frequency. This oversimplifies PWM harmonic content and does not allow to study effects of interactions between different PWM harmonics. More recent references typically treat stator currents in a generic way, allowing multiple time harmonics, but assuming that they are located at frequencies that are integer multiples of the fundamental frequency [20–22]. This assumption can be found even in papers that specifically model PWM supplied high-speed machines and compare their performance against machines driven by other modulation strategies [23]. Although this assumption can indeed hold for PWM supply, this is not always the case. Namely, frequencies of PWM harmonics are determined by the switching frequency. In high-speed applications, inverter switching losses can be very high. To limit these losses, switching frequency in practice can be set to values that do not give integer frequency modulation ratio, violating the previously discussed assumption of integer orders of PWM harmonics. The work presented in this study does not put any assumption on the harmonic content of stator currents, but treats it as a function of the arbitrary switching frequency.

To accurately assess the performance of a high-speed machine supplied by a PWM inverter, interactions caused by higher order time and spatial harmonics need to be properly addressed to reflect conditions corresponding to PWM supply. In contrast to another often used assumption, applied, for instance in [24], the phase shift between current harmonics in different phases of a PWM supplied machine is not determined by the absolute harmonic order, but by the position of the harmonic in a sideband or a baseband [25]. As the phase shift determines the rotational sequence of traveling waves generated by each PWM harmonic, it has a significant influence on the machine performance. The model derived in this study applies this phase shift correctly, accurately representing conditions under PWM supply. Furthermore, all spatial harmonics of both the rotor and the stator field are taken into account, which is often omitted by authors who solely focus on the proper implementation of PWM harmonics, as done in [26,27].

Starting from models based on the harmonic modeling method, presented previously by the same author in [28,29], this paper develops an extensive study for the performance analysis of high-speed PWM supplied electric machines. Effects related to both spatial harmonics (determined by the machine structure) and time harmonics (determined by the modulation strategy and switching frequency) are properly included. This fills the gaps in the existing work which, as discussed previously, typically focuses only on one of these 2 aspects. Rotor eddy current losses and electromagnetic torque, as main indicators of the machine performance, are formulated in terms of the specific time and spatial harmonics which actually exist in a given machine. This makes the implementation of analytical expressions derived in this study more straightforward in comparison to typically used expressions which include multiple infinite summations over generic time and spatial harmonics, as done, for instance, in [21,30].

2. Magnetic Field in High-Speed PM Machines Supplied by PWM Inverters

The analysis shown in this study utilizes previously developed models of the magnetic field in high-speed machines. The field generated by stator currents and the field created by the magnet are modeled separately. Both models include effects of eddy currents in solid conducting regions in the rotor, and they are developed in the polar coordinate system. Models assume two-dimensional (2D) magnetic field distribution. Therefore, the magnetic field strength H [A/m] and the magnetic flux density B [T] have only radial and circumferential components, while the induced electric field E [V/m] and the magnetic vector potential A [Wb/m] have only the axial component.

A slotted high-speed PM machine with a diametrically magnetized magnet, displayed in Figure 1, is used as a benchmark topology to illustrate the presented method.

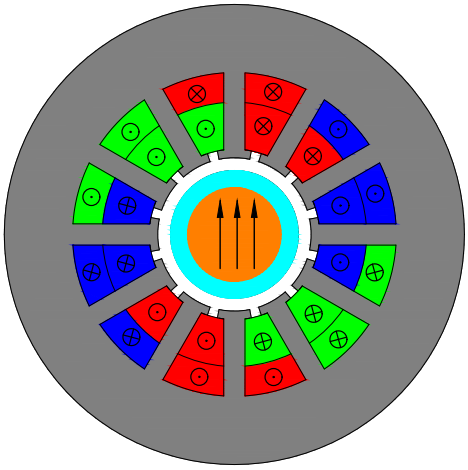

Figure 1. Cross section of the benchmark high-speed PM machine. Adapted with permission from ref. [31]. Copyright 2015 IEEE.

Arrows in the rotor indicate the magnetization pattern which is commonly referred to as diametrical magnetization. The magnet is contained in a retaining sleeve made of a material with high mechanical strength. Parameters of the machine are given in Table 1.

If the rotor magnetization is set to zero, the topology shown in Figure 1 resembles the structure of solid rotor or copper-coated solid rotor high-speed induction machines [32,33]. Therefore, qualitative findings of the analysis presented in this study can also be applied to induction machines, if only the field associated with PWM stator currents is considered.

Table 1. Dimensions and parameters of the benchmark high-speed PM machine.

Parameter	Value	Unit
Fundamental frequency	4	kHz
Magnet recoil permeability	1.035	-
Magnet conductivity	6.25×10^5	S/m
Magnet remanence	1.19	T
Sleeve relative permeability	1	-
Sleeve conductivity	8.33×10^5	S/m
Slot opening width	7.5	degree
Active length	25	mm
Magnet radius	5.5	mm
Sleeve outer radius	7.5	mm
Stator inner radius	9	mm
Slot outer radius	19	mm

As derived in [28], the axial component of the magnetic vector potential in the air-gap of a high-speed PM machine, created by 3-phase currents supplied by a pulse-width modulated voltage source inverter (PWM VSI), can be expressed as

$$\bar{A}_z^{\mathrm{ar}}(r,\theta_\mathrm{r},t) = \sum_{L=-\infty}^{\infty} \sum_{\substack{m=0 \\ m>0}}^{\infty} \sum_{n=-\infty}^{\infty} \hat{\bar{A}}_z^{\mathrm{ar}}(r,L,m,n) e^{j((3L-n)(\theta_\mathrm{r}+\theta_0)+(m\cdot m_\mathrm{f}+3L)\omega_0 t)}, \tag{1}$$

where $\hat{\bar{A}}_z^{\mathrm{ar}}$ is the complex harmonic peak value, r [m] is the radial coordinate, θ_r [rad] is the circumferential coordinate in the reference frame of the rotor, and θ_0 [rad] is the initial rotor position. Index L is an integer, while m_f represents the frequency modulation ratio of the inverter (the ratio between the switching and the fundamental frequency). Indices m and n indicate baseband (for $m = 0$) and sideband (for $m > 0$) harmonics in the PWM inverter output voltage, as shown in Figure 2. Combination $(m = 0,\ n = 1)$ represents the fundamental component. The fundamental angular frequency of armature currents is indicated by ω_0 [rad/s], while t stands for time. Expression equivalent to (1) can be used to model magnetic field in the air-gap of high-speed solid rotor induction machine. Namely, instead of assuming that the mechanical speed of the rotor is ω_0, as done while deriving (1) in [28], any other rotor mechanical speed can be assumed.

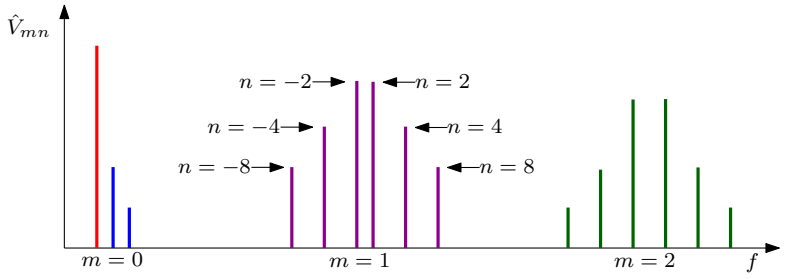

Figure 2. Harmonic components of PWM VSI line-to-line output voltages.

Analytical expressions for the output voltage of a 3-phase inverter with various modulation strategies can be found in [25]. By transforming these expressions, the amplitude of any harmonic component of phase voltage in Y connected 3-phase machine can be formulated as

$$\hat{V}_{mn}^{\mathrm{P}} = \frac{8V_{\mathrm{DC}}m_\mathrm{f}}{3\pi(m\cdot m_f+n)} J_n\left(\frac{(m\cdot m_f+n)\pi m_\mathrm{a}}{2m_\mathrm{f}}\right) \sin\left([m+n]\frac{\pi}{2}\right) \sin^2\left(n\frac{\pi}{3}\right), \tag{2}$$

where V_{DC} [V] is the inverter DC bus voltage, and m_a is the amplitude modulation ratio of the inverter. Term J_n is the Bessel function of the first kind of order n. Equation (2)

corresponds to asymmetrical regular PWM sampling modulation strategy. While other modulation strategies give different amplitudes of individual harmonics, all of them allow only components for which the following condition is fulfilled

$$n \neq 3M,\ M \in \mathbb{Z}, \tag{3}$$

as seen in (2). Index n determines the phase shift between currents corresponding to the same harmonic component in different phases [25]. Therefore, condition (3) expresses the fact that in stator windings there are no harmonic components corresponding to zero-sequence currents. Although this is always true if phase windings are connected in Y connection, it would also hold for the inverter fed machine in Δ connection, since it can be shown that harmonic components for which n is a multiple of 3 cannot be present in the inverter line-to-line output voltages [25]. Furthermore, as spatial harmonics in (1) are defined as $(3L - n)$, it can be concluded that spatial harmonics with the order which is a multiple of 3 do not contribute to the magnetic field of stator currents. As n gives the phase shift between different phases, it defines in which direction the resultant stator magnetic field corresponding to that harmonic component rotates. If n takes one of the following values

$$n = 3M + 1,\ M \in \mathbb{Z}, \tag{4}$$

the considered harmonic component gives so-called positive sequence and the stator magnetic field corresponding to that harmonic component and the fundamental spatial harmonic rotates in the same direction as the rotor. Naturally, the fundamental component of stator currents is of a positive sequence. Conversely, if n takes one of the following values

$$n = 3M - 1,\ M \in \mathbb{Z}, \tag{5}$$

the considered harmonic component gives so-called negative sequence and the stator field corresponding to that harmonic component and the fundamental spatial harmonic rotates in the direction opposite of the rotor.

Similarly to (1), as derived in [29], the axial component of the magnetic vector potential in the air-gap of a high-speed 3-phase PM machine created by a magnet with diametrical magnetization is given by

$$A_z^{\mathrm{nl}}(r, \theta_\mathrm{r}, t) = \sum_{k_\mathrm{p}=-\infty}^{\infty} \hat{A}_z^{\mathrm{nl},0}(r, k_\mathrm{p}) e^{j\left(k_\mathrm{p}\theta_\mathrm{r} + l_\mathrm{p}(k_\mathrm{p})\theta_0 + l_\mathrm{p}(k_\mathrm{p})\omega_0 t\right)}, \tag{6}$$

where $\hat{A}_z^{\mathrm{nl},0}$ is the complex harmonic peak value defined for a single initial position of the rotor, k_p is the spatial harmonic index, and l_p is time harmonic index of the PM field in the rotor reference frame. For the benchmark topology shown in Figure 1, existing k_p and associated l_p are shown in Table 2.

Table 2. Values of k_p for the benchmark machine with corresponding values of l_p.

k_p	±1	±11	±13	±23	±25	±35	±37	±47	±49
l_p	0	±12	±12	±24	±24	±36	±36	±48	±48

In most general terms, k_p takes values ± 1 for the fundamental harmonic, and $\pm k_\mathrm{pm}$ for higher order spatial harmonics, where k_pm is defined as [29]

$$k_\mathrm{pm} = pN_\mathrm{s} \pm 1,\ p \in \mathbb{N}, \tag{7}$$

with N_s being the number of slots. As the number of slots in 3-phase machines is always a multiple of 3, it follows that the magnetization pattern shown in Figure 1 cannot generate

spatial harmonics with orders which are multiples of 3. For a given k_p, l_p is always the closest integer which is a multiple of 3. Due to fixed relation between k_p and l_p, it is possible to describe field variations in both space and time using a single summation term, as shown in (6). Mathematically, this implies that each spatial harmonic, as seen in the rotor reference frame, varies with a single frequency. Physically, this means that each spatial harmonic is described by a single traveling wave that moves at a fixed speed. This comes as a consequence of having only the fundamental spatial component in the rotor magnetization. Higher-order spatial harmonics result from the interaction between the fundamental component of the magnetization and stator slots. The fact that each spatial harmonic is associated with a single traveling wave has a significant effect on the machine performance at no-load conditions, as will be discussed later.

In a 2D model, the magnetic flux density in the air-gap is expressed using its radial component B_r and the circumferential component of the magnetic field strength H_θ as

$$\vec{B} = B_r \vec{i}_r + \mu_0 H_\theta \vec{i}_\theta, \tag{8}$$

where μ_0 [H/m] is the permeability of vacuum, and $\vec{i}_r$ and $\vec{i}_\theta$ are unit vectors in the radial and circumferential direction, respectively. On the other hand, the vector potential $\vec{A}$ is defined as [34]

$$\vec{B} = \nabla \times \vec{A}. \tag{9}$$

For a 2D approximation, field quantities are invariant in the axial direction. As only the axial component A_z is present, (9) simplifies to

$$\vec{B} = \frac{1}{r}\frac{\partial A_z}{\partial \theta_r}\vec{i}_r - \frac{\partial A_z}{\partial r}\vec{i}_\theta. \tag{10}$$

By comparing (8) and (10), B_r and H_θ can be expressed as a function of A_z in the reference frame of the rotor as

$$B_r = \frac{1}{r}\frac{\partial A_z(r,\theta_\mathrm{r},t)}{\partial \theta_r}\ ;\ H_\theta = -\frac{1}{\mu_0}\frac{\partial A_z(r,\theta_\mathrm{r},t)}{\partial r}. \tag{11}$$

By combining (9) with Faraday's law given by (A3) in Appendix A, the axial component of the induced electric field can be expressed as

$$E_z = -\frac{\partial A_z(r,\theta_\mathrm{r},t)}{\partial t}. \tag{12}$$

The estimation of eddy current losses, as one of the main indicators of electric machine performance, requires volume integration. The field solution in polar coordinates with included eddy current effects contains Bessel functions [28,29]. Performing the volume integral of Bessel functions can represent a significant challenge [35,36]. However, by using Poynting's theorem, eddy current losses can be calculated using a surface integral. Generalized Poynting's theorem for a structure containing the imposed current density $\vec{J}_\mathrm{i}$ (representing stator currents) and permanent magnets with the remanent flux density $\vec{B}_\mathrm{rem}$, can be expressed, as shown in [24] and derived in Appendix A, by

$$\begin{aligned} -\oint_S \left(\vec{E}\times\vec{H}\right)\cdot\vec{n}\,\mathrm{d}S = \frac{\mu_0}{2}\frac{\partial}{\partial t}\int_V \mu_\mathrm{r}|\vec{H}|^2\mathrm{d}V + \int_V \sigma|\vec{E}|^2\mathrm{d}V \\ + \int_V \vec{H}\cdot\frac{\partial \vec{B}_\mathrm{rem}}{\partial t}\mathrm{d}V + \int_V \vec{E}\cdot\vec{J}_\mathrm{i}\mathrm{d}V, \end{aligned} \tag{13}$$

where μ_r is the relative permeability, S is a closed surface surrounding volume V, and $\vec{n}$ is the outward normal on surface S. All field quantities in (13) are in the real domain. If the

goal is to calculate rotor eddy current losses, S can be chosen as a closed cylindrical surface located in the air gap and fixed to the reference frame of the rotor. In that case, the last term on the right side of (13) vanishes, as there is no externally imposed current density enclosed by S. Furthermore, the second last term on the right side of (13) also vanishes, even in the case of PM machines, as the volume V rotates together with the rotor magnets and there is no variation of the remanent flux density. For a 2D model used in this work, expression (13) therefore transforms into

$$\int_{S_r} E_z(r = r_S, \theta_r) H_\theta(r = r_S, \theta_r) \mathrm{d}S_r = \frac{1}{2\mu_0} \frac{\partial}{\partial t} \int_V \frac{B_r^2}{\mu_r} \mathrm{d}V + \frac{\mu_0}{2} \frac{\partial}{\partial t} \int_V \mu_r H_\theta^2 \mathrm{d}V + \int_V \sigma E_z^2 \mathrm{d}V, \tag{14}$$

where S_r is the part of surface S with the normal $\vec{n}$ directed in the radial direction, where the integral over the closed surface gives a non-zero result. Parameter r_S [m] represents the radius in the air-gap at which S_r is located. The first 2 terms on the right side of (14) represent the rate of change of the energy stored in the magnetic field, while the last term represents eddy current losses generated inside the considered volume V. Therefore, by using (14), only the time-independent component of rotor eddy current losses can be calculated. In that case, the first 2 terms on the right side vanish, and average eddy current losses can be determined by performing the surface integral on the left side of expression (14).

By using Maxwell's stress tensor [34], the electromagnetic torque created by 2D magnetic field can be obtained by evaluating the following surface integral [37]

$$T = \frac{r_S}{\mu_0} \int_{S_r} B_r(r = r_S, \theta_r) B_\theta(r = r_S, \theta_r) \mathrm{d}S_r, \tag{15}$$

with S_r and r_S representing the same surface and same radius in the air-gap as in (14), respectively. Like in (14), both radial and circumferential components of flux density B_r and B_θ in (15) are real numbers. With all significant aspects defined in this section, it is now possible to analyze machine performance using previously established field solution and accompanying relations.

3. Analysis of High-Speed Machine Performance Due to PWM Currents

As seen in (1), the field of stator currents is the combination of field components created by different PWM harmonics shown in Figure 2. This is described by the summation over m and n. Interactions between different PWM harmonics cause significant variations in instantaneous values of the electromagnetic torque [26,27] and rotor eddy current losses, obtained by (15) and (14), respectively. To illustrate these interactions, 2 angular frequencies ω_1 and ω_2 can be introduced as

$$\omega_1 = (m_1 \cdot m_f + n_1)\omega_0 \quad ; \quad \omega_2 = (m_2 \cdot m_f + n_2)\omega_0. \tag{16}$$

All terms in (14) and (15) contain a product of 2 field quantities. To model interactions between these quantities caused by different PWM harmonics, it is useful to introduce generic quantities $\bar{G}_1$ and $\bar{G}_2$. When referring to the right side of (14), then $\bar{G}_1 = \bar{G}_2$. Conversely, when referring to the left side of (14) or the right side of (15), then $\bar{G}_1 \neq \bar{G}_2$. $\bar{G}_1$ and $\bar{G}_2$ are created simultaneously by both PWM components with angular frequencies ω_1 and ω_2 given by (16). By dropping the summation over m and n, and replacing it by the exact terms corresponding to ω_1 and ω_2, the form of $\bar{G}_1$ and $\bar{G}_2$ given by (1) becomes

$$\bar{G}_1 = \sum_{L_1=-\infty}^{\infty} \Big(\hat{\bar{G}}_1(L_1, m_1, n_1) e^{j((3L_1-n_1)(\theta_r+\theta_0)+(m_1 \cdot m_f+3L_1)\omega_0 t)} + \hat{\bar{G}}_1(L_1, m_2, n_2) e^{j((3L_1-n_2)(\theta_r+\theta_0)+(m_2 \cdot m_f+3L_1)\omega_0 t)} \Big), \tag{17}$$

and

$$\bar{G}_2 = \sum_{L_2=-\infty}^{\infty} \Big(\hat{\bar{G}}_2(L_2, m_1, n_1) e^{j((3L_2-n_1)(\theta_r+\theta_0)+(m_1 \cdot m_f+3L_2)\omega_0 t)} + \hat{\bar{G}}_2(L_2, m_2, n_2) e^{j((3L_2-n_2)(\theta_r+\theta_0)+(m_2 \cdot m_f+3L_2)\omega_0 t)} \Big), \tag{18}$$

where $\hat{\bar{G}}_1$ and $\hat{\bar{G}}_2$ are the generic complex harmonic peak values. Generic quantities G_1 and G_2, which have to be inserted into (14) and (15), are real numbers—real parts of corresponding quantities $\bar{G}_1$ and $\bar{G}_2$. Therefore, it can be written

$$G_1 = \Re(\bar{G}_1) = \frac{1}{2}(\bar{G}_1 + \bar{G}_1^*) \quad ; \quad G_2 = \Re(\bar{G}_2) = \frac{1}{2}(\bar{G}_2 + \bar{G}_2^*), \tag{19}$$

where $*$ stands for the complex conjugation and $\Re$ is the real part of a complex number.

Due to the shape of the closed surface S, all integrals in (14) and (15) assume integration in the circumferential direction in the range from $-\pi$ and π. Therefore, a generic integral I^{ar}, contained in all previously introduced surface and volume integrals, can be defined as

$$I^{\mathrm{ar}} = \int_{-\pi}^{\pi} G_1 G_2 \mathrm{d}\theta_r. \tag{20}$$

By inserting (19) into (20), I^{ar} can be further developed as

$$\begin{aligned} I^{\mathrm{ar}} &= \frac{1}{4}\int_{-\pi}^{\pi} (\bar{G}_1 + \bar{G}_1^*)(\bar{G}_2 + \bar{G}_2^*)\mathrm{d}\theta_r = \frac{1}{4}\int_{-\pi}^{\pi} \left(\bar{G}_1\bar{G}_2 + \bar{G}_1\bar{G}_2^* + (\bar{G}_1\bar{G}_2 + \bar{G}_1\bar{G}_2^*)^*\right)\mathrm{d}\theta_r \\ &= \frac{1}{2}\int_{-\pi}^{\pi} \Re(\bar{G}_1\bar{G}_2)\mathrm{d}\theta_r + \frac{1}{2}\int_{-\pi}^{\pi} \Re(\bar{G}_1\bar{G}_2^*)\mathrm{d}\theta_r = I_1^{\mathrm{ar}} + I_2^{\mathrm{ar}}. \end{aligned} \tag{21}$$

By inserting (17) and (18) into (21), qualitative spectral analysis of the instantaneous torque and rotor eddy current losses can be performed, in order to reveal results of the mutual interaction between different PWM harmonics in the stator voltages and currents. If (17) and (18) are inserted into (21), the following expression can be derived for integral I_1^{ar}

$$\begin{aligned} I_1^{\mathrm{ar}} &= \frac{1}{2}\int_{-\pi}^{\pi} \Re(\bar{G}_1\bar{G}_2)\mathrm{d}\theta_r = \frac{1}{2}\sum_{L_1=-\infty}^{\infty}\sum_{L_2=-\infty}^{\infty} \\ &\cdot \int_{-\pi}^{\pi} \Bigg(\Re\Big(\hat{\bar{G}}_1(L_1, m_1, n_1)\hat{\bar{G}}_2(L_2, m_1, n_1) e^{j((3(L_1+L_2)-2n_1)(\theta_r+\theta_0)+(2m_1 \cdot m_f+3(L_1+L_2))\omega_0 t)}\Big) \\ &+ \Re\Big(\hat{\bar{G}}_1(L_1, m_1, n_1)\hat{\bar{G}}_2(L_2, m_2, n_2) e^{j((3L_1-n_1+3L_2-n_2)(\theta_r+\theta_0)+((m_1+m_2)m_f+3(L_1+L_2))\omega_0 t)}\Big) \\ &+ \Re\Big(\hat{\bar{G}}_1(L_1, m_2, n_2)\hat{\bar{G}}_2(L_2, m_1, n_1) e^{j((3L_1-n_2+3L_2-n_1)(\theta_r+\theta_0)+((m_2+m_1)m_f+3(L_1+L_2))\omega_0 t)}\Big) \\ &+ \Re\Big(\hat{\bar{G}}_1(L_1, m_2, n_2)\hat{\bar{G}}_2(L_2, m_2, n_2) e^{j((3(L_1+L_2)-2n_2)(\theta_r+\theta_0)+(2m_2 \cdot m_f+3(L_1+L_2))\omega_0 t)}\Big)\Bigg)\mathrm{d}\theta_r \\ &= I_1^{\mathrm{ar,a}} + I_1^{\mathrm{ar,b}} + I_1^{\mathrm{ar,c}} + I_1^{\mathrm{ar,d}}. \end{aligned} \tag{22}$$

The integration of a periodic function over an integer number of periods results in zero. Therefore, integrals in (22) give a non-zero result only if functions under these integrals are independent of θ_r. Consequently, integrals $I_1^{ar,a}$ and $I_1^{ar,d}$ take non-zero values if the following conditions are met, respectively

$$L_1 + L_2 = \frac{2n_1}{3} \quad ; \quad L_1 + L_2 = \frac{2n_2}{3}. \tag{23}$$

Since L_1 and L_2 are integers, and n cannot be a multiple of 3, as stated by (3), conditions given by (23) are never fulfilled. Consequently, integrals $I_1^{ar,a}$ and $I_1^{ar,d}$ always have a zero result and do not contribute to I_1^{ar}. Integrals $I_1^{ar,b}$ and $I_1^{ar,c}$ take non-zero values if

$$L_1 + L_2 = \frac{n_1 + n_2}{3}. \tag{24}$$

Condition (24) states that spatial harmonics of the same order within G_1 and G_2, caused by different PWM harmonic components in stator currents, interact mutually. Since spatial waveforms corresponding to the same spatial harmonic in the air-gap, but to 2 different PWM harmonics, move around the machine circumference at different speeds, the result of this interaction is time dependent. By inserting (24) into (22) and taking into account (16), the frequency associated to non-zero terms of I_1^{ar} can be expressed as

$$\omega_{I_1} = \Big((m_1 + m_2)m_f + 3(L_1 + L_2)\Big)\omega_0 = \Big((m_1 + m_2)m_f + n_1 + n_2\Big)\omega_0 = \omega_1 + \omega_2. \tag{25}$$

Therefore, (22) can be rewritten as

$$I_1^{ar} = \pi \sum_{L_1,L_2} \Re\Bigg(\Big(\hat{\bar{G}}_1(L_1, m_1, n_1)\hat{\bar{G}}_2(L_2, m_2, n_2) + \hat{\bar{G}}_1(L_1, m_2, n_2)\hat{\bar{G}}_2(L_2, m_1, n_1)\Big) e^{j(\omega_1+\omega_2)t} \Bigg), \tag{26}$$

where only combinations of L_1 and L_2 which satisfy (24) are allowed. Since both L_1 and L_2 are defined as integers, the right side of (24) needs always to give an integer. If expressions (4) and (5) are inserted into (24), it can be seen that this will be the case only if one of the considered PWM harmonic components gives positive sequence currents, and the other one gives negative sequence currents. Therefore, only these combinations of PWM harmonics in the stator currents actually contribute to I_1^{ar}. If (17) and (18) are again inserted into (21), the following expression can be derived for integral I_2^{ar}

$$\begin{aligned} I_2^{ar} &= \frac{1}{2}\int_{-\pi}^{\pi} \Re(\bar{G}_1\bar{G}_2^*)\mathrm{d}\theta_r = \frac{1}{2}\sum_{L_1=-\infty}^{\infty}\sum_{L_2=-\infty}^{\infty} \\ &\cdot \int_{-\pi}^{\pi} \Bigg(\Re\Big(\hat{\bar{G}}_1(L_1, m_1, n_1)\hat{\bar{G}}_2^*(L_2, m_1, n_1)e^{j(3(L_1-L_2)(\theta_r+\theta_0)+3(L_1-L_2)\omega_0 t)}\Big) \\ &+ \Re\Big(\hat{\bar{G}}_1(L_1, m_1, n_1)\hat{\bar{G}}_2^*(L_2, m_2, n_2)e^{j((3L_1-n_1-(3L_2-n_2))(\theta_r+\theta_0)+((m_1-m_2)m_f+3(L_1-L_2))\omega_0 t)}\Big) \\ &+ \Re\Big(\hat{\bar{G}}_1(L_1, m_2, n_2)\hat{\bar{G}}_2^*(L_2, m_1, n_1)e^{j((3L_1-n_2-(3L_2-n_1))(\theta_r+\theta_0)+((m_2-m_1)m_f+3(L_1-L_2))\omega_0 t)}\Big) \\ &+ \Re\Big(\hat{\bar{G}}_1(L_1, m_2, n_2)\hat{\bar{G}}_2^*(L_2, m_2, n_2)e^{j(3(L_1-L_2)(\theta_r+\theta_0)+3(L_1-L_2)\omega_0 t)}\Big)\Bigg)\mathrm{d}\theta_r \\ &= I_2^{ar,a} + I_2^{ar,b} + I_2^{ar,c} + I_2^{ar,d}. \end{aligned} \tag{27}$$

Terms $I_2^{\mathrm{ar,a}}$ and $I_2^{\mathrm{ar,d}}$ exist when the following condition is fulfilled

$$L_1 = L_2. \tag{28}$$

This condition implies that the frequency of $I_2^{\mathrm{ar,a}}$ and $I_2^{\mathrm{ar,d}}$ is zero. Therefore, these 2 terms sum up time independent contributions of individual PWM harmonics, as

$$I_2^{\mathrm{ar,a}} + I_2^{\mathrm{ar,d}} = \pi \sum_{L=-\infty}^{\infty} \Re\Big(\hat{\bar{G}}_1(L, m_1, n_1)\hat{\bar{G}}_2^*(L, m_1, n_1) + \hat{\bar{G}}_1(L, m_2, n_2)\hat{\bar{G}}_2^*(L, m_2, n_2)\Big). \tag{29}$$

$I_2^{\mathrm{ar,b}}$ and $I_2^{\mathrm{ar,c}}$ take non-zero values when the following conditions hold, respectively

$$L_1 - L_2 = \frac{n_1 - n_2}{3} \quad ; \quad L_1 - L_2 = \frac{n_2 - n_1}{3}. \tag{30}$$

Expression (30) again illustrates the interaction of same spatial harmonic components within G_1 and G_2, caused by different PWM harmonics in stator currents. By inserting the first equation of (30) into (27) and taking into account (16), the frequency associated to $I_2^{\mathrm{ar,b}}$ can be expressed as

$$\omega_{I_2^{\mathrm{b}}} = \Big((m_1 - m_2)m_{\mathrm{f}} + 3(L_1 - L_2)\Big)\omega_0 = \Big((m_1 - m_2)m_{\mathrm{f}} + n_1 - n_2\Big)\omega_0 = \omega_1 - \omega_2. \tag{31}$$

Similarly, by inserting the second equation of (30) into (27), the frequency associated to $I_2^{\mathrm{ar,c}}$ can be expressed as

$$\omega_{I_2^{\mathrm{c}}} = \Big((m_2 - m_1)m_{\mathrm{f}} + 3(L_1 - L_2)\Big)\omega_0 = \Big((m_2 - m_1)m_{\mathrm{f}} + n_2 - n_1\Big)\omega_0 = \omega_2 - \omega_1. \tag{32}$$

Now it can be written

$$I_2^{\mathrm{ar,b}} = \pi \sum_{L_1, L_2} \Re\Big(\hat{\bar{G}}_1(L_1, m_1, n_1)\hat{\bar{G}}_2^*(L_2, m_2, n_2)e^{j(\omega_1 - \omega_2)t}\Big), \tag{33}$$

where only combinations of L_1 and L_2 which satisfy the first equation of (30) are allowed. Similarly to (33), it can be written

$$I_2^{\mathrm{ar,c}} = \pi \sum_{L_1, L_2} \Re\Big(\hat{\bar{G}}_1(L_1, m_2, n_2)\hat{\bar{G}}_2^*(L_2, m_1, n_1)e^{j(\omega_2 - \omega_1)t}\Big), \tag{34}$$

where only combinations of L_1 and L_2 which satisfy the second equation of (30) are allowed. Both L_1 and L_2 are defined as integers, and consequently right sides of (30) need always to give integers. If expressions (4) and (5) are inserted into (30), it can be seen that this will be the case only if both considered PWM harmonic components give either positive or negative sequence currents. Therefore, only these combinations of time harmonics in the stator currents actually contribute to $I_2^{\mathrm{ar,b}}$ and $I_2^{\mathrm{ar,c}}$.

Finally, by combining (26), (29), (33), and (34), the general form of expression (20) in the presence of all PWM harmonics can be written as

$$
\begin{aligned}
I^{\mathrm{ar}} = \int_{-\pi}^{\pi} G_1 G_2 \mathrm{d}\theta_{\mathrm{r}} = \pi \sum_{L=-\infty}^{\infty} \sum_{\substack{m=0 \\ m>0}}^{\infty} \sum_{\substack{n=1 \\ n=-\infty}}^{\infty} \Re\left(\hat{\bar{G}}_{1L}^{mn} \hat{\bar{G}}_{2L}^{mn*}\right) \\
+\pi \sum_{L_1,L_2} \sum_{m_1,m_2} \sum_{n_1,n_2} \Re\left(\hat{\bar{G}}_{1L_1}^{m_1 n_1} \hat{\bar{G}}_{2L_2}^{m_2 n_2} e^{j(\omega_1+\omega_2)t}\right), \text{ for } L_1 + L_2 = \frac{n_1+n_2}{3} \\
+\pi \sum_{L_1,L_2} \sum_{m_1,m_2} \sum_{n_1,n_2} \Re\left(\hat{\bar{G}}_{1L_1}^{m_2 n_2} \hat{\bar{G}}_{2L_2}^{m_1 n_1} e^{j(\omega_1+\omega_2)t}\right), \text{ for } L_1 + L_2 = \frac{n_1+n_2}{3} \\
+\pi \sum_{L_1,L_2} \sum_{m_1,m_2} \sum_{n_1,n_2} \Re\left(\hat{\bar{G}}_{1L_1}^{m_1 n_1} \hat{\bar{G}}_{2L_2}^{m_2 n_2 *} e^{j(\omega_1-\omega_2)t}\right), \text{ for } L_1 - L_2 = \frac{n_1-n_2}{3} \\
+\pi \sum_{L_1,L_2} \sum_{m_1,m_2} \sum_{n_1,n_2} \Re\left(\hat{\bar{G}}_{1L_1}^{m_2 n_2} \hat{\bar{G}}_{2L_2}^{m_1 n_1 *} e^{j(\omega_2-\omega_1)t}\right), \text{ for } L_1 - L_2 = \frac{n_2-n_1}{3}.
\end{aligned} \tag{35}
$$

Each of last 4 terms in (35) models interactions between all pairs of PWM harmonics which satisfy conditions specified at the end of the corresponding line. Furthermore, a simplified notation is used in (35), where $\hat{\bar{G}}(L, m, n)$ is written as $\hat{\bar{G}}_L^{mn}$.

Expression (35) has been derived assuming that the conducting regions on the rotor move with respect to the stator at the angular speed ω_0, which is the same as the fundamental angular frequency of stator currents. This is because the original model for the magnetic field of PWM harmonics, derived in [28], was applied on a PM synchronous machine. However, the conclusion about frequencies at which components in (35) appear can be generalized regardless of the mechanical speed of conducting regions. If the rotor movement occurs at arbitrary angular speed ω_{mech} [rad/s], the angular coordinate of any point expressed in the fixed (θ_{s}) and moving (θ_{c}) reference frames can be related through ω_{mech} and the initial rotor position θ_0 (rotor position for $t = 0$) as [38]

$$
\theta_{\mathrm{s}} = \theta_{\mathrm{c}} + \omega_{\mathrm{mech}} t + \theta_0. \tag{36}
$$

The argument of the generic field quantity, relevant for the form of the generic integral I^{ar}, then becomes [28]

$$
\begin{aligned}
\arg(\bar{G}) &= (3L - n)\theta_{\mathrm{s}} + (m \cdot m_{\mathrm{f}} + n)\omega_0 t \\
&= (3L - n)(\theta_{\mathrm{c}} + \theta_0) + (3L - n)\omega_{\mathrm{mech}} t + (m \cdot m_{\mathrm{f}} + n)\omega_0 t.
\end{aligned} \tag{37}
$$

Different terms in generic integral I^{ar} take non-zero values only when the dependency on θ_{c} (or θ_{r}) vanishes, as shown previously. Consequently, if G_1 and G_2 are expressed using (37), the dependency on ω_{mech} also vanishes from non-zero terms of I^{ar}. The dependency on θ_{c} and ω_{mech} in (37) is identical, as they are both multiplied by the same term—spatial harmonic $(3L - n)$. Therefore, previously derived analysis is independent of the mechanical speed of conducting regions. This makes it applicable for the blocked rotor test, as well as for solid rotor induction machines. If formulation (37) is used, together with frequencies ω_1 and ω_2 defined by (16), it can be shown that same results for frequencies of different terms present in I^{ar} are obtained as with (25), (31), and (32).

Each term in Poynting's theorem (14) contains integral (35), which is dependent on time. Therefore, in the case of multiple time harmonics in stator currents (PWM excitation), all terms are present on the right side of (35), and the instantaneous rotor eddy current losses cannot be obtained by performing the surface integral on the left side. The main advantage of using Poynting's theorem—avoiding the volume integration of the field solution based on Bessel functions, seems to be lost. However, from the point of view of the temperature rise in the rotor, only the average value of the rotor eddy current losses is relevant. The average value is given by the first term in (35), since all other terms, if present, give sinusoidal variations in time. As already discussed, by considering only the constant part of (35), the contribution of the first 2 terms on the right side of (14) vanishes. By

replacing $\bar{G}_1$ with the axial component of the induced electric field $\bar{E}_z$, and $\bar{G}_2$ with the circumferential component of the magnetic field strength $\bar{H}_\theta$ in (35), average rotor eddy current losses caused by multiple time harmonics due to PWM currents can be obtained, by performing the surface integral on the left side of (14), as

$$P_{\text{eddy}}^{\text{ar,av}} = \pi l_s r_S \sum_{L=-\infty}^{\infty} \sum_{\substack{m=0 \\ m>0}}^{\infty} \sum_{\substack{n=1 \\ n=-\infty}}^{\infty} \Re\left(\hat{\bar{E}}_z(r=r_S, L, m, n)\hat{\bar{H}}_\theta^*(r=r_S, L, m, n)\right), \tag{38}$$

where l_s [m] is the active length of the machine. Similarly, by replacing $\bar{G}_1$ with the radial component of the magnetic flux density $\bar{B}_r$, and $\bar{G}_2$ with the circumferential component of the magnetic field strength $\bar{H}_\theta$ in (35), instantaneous torque caused by multiple time harmonics due to PWM currents can be obtained, by evaluating (15) as

$$\begin{aligned} T^{\text{ar}}(t) = \pi l_s r_S^2 \Bigg(& \sum_{L=-\infty}^{\infty} \sum_{\substack{m=0 \\ m>0}}^{\infty} \sum_{\substack{n=1 \\ n=-\infty}}^{\infty} \Re\left(\hat{B}_{rL}^{mn}\hat{H}_{\theta L}^{mn*}\right) \\ & + \sum_{L_1,L_2} \sum_{m_1,m_2} \sum_{n_1,n_2} \Re\left(\hat{B}_{rL_1}^{m_1n_1}\hat{H}_{\theta L_2}^{m_2n_2} e^{j(\omega_1+\omega_2)t}\right), \quad \text{for } L_1 + L_2 = \frac{n_1+n_2}{3} \\ & + \sum_{L_1,L_2} \sum_{m_1,m_2} \sum_{n_1,n_2} \Re\left(\hat{B}_{rL_1}^{m_2n_2}\hat{H}_{\theta L_2}^{m_1n_1} e^{j(\omega_1+\omega_2)t}\right), \quad \text{for } L_1 + L_2 = \frac{n_1+n_2}{3} \\ & + \sum_{L_1,L_2} \sum_{m_1,m_2} \sum_{n_1,n_2} \Re\left(\hat{B}_{rL_1}^{m_1n_1}\hat{H}_{\theta L_2}^{m_2n_2*} e^{j(\omega_1-\omega_2)t}\right), \quad \text{for } L_1 - L_2 = \frac{n_1-n_2}{3} \\ & + \sum_{L_1,L_2} \sum_{m_1,m_2} \sum_{n_1,n_2} \Re\left(\hat{B}_{rL_1}^{m_2n_2}\hat{H}_{\theta L_2}^{m_1n_1*} e^{j(\omega_2-\omega_1)t}\right), \quad \text{for } L_1 - L_2 = \frac{n_2-n_1}{3} \Bigg). \end{aligned} \tag{39}$$

The torque given by (39) is the total torque in the case of a solid rotor or copper-coated solid rotor high-speed induction machines. In the case of PM machines, to obtain the total torque, the result of (39) has to be added to the no-load torque (the result of the interaction between the rotor magnet and stator slots) and the torque resulting from the interaction between the rotor magnet and stator PWM currents, as will be shown later.

4. FEM Validation of High-Speed Machine Performance Due to PWM Currents

To verify models derived in Section 3, a finite element model of the benchmark machine is created in Flux2D 12.2 software. To illustrate only the effects of PWM currents, the remanent flux density of the magnet is set to zero. The current waveform shown in Figure 3 is used. It corresponds to the switching frequency of 40 kHz, therefore to the frequency modulation ratio $m_f = 10$.

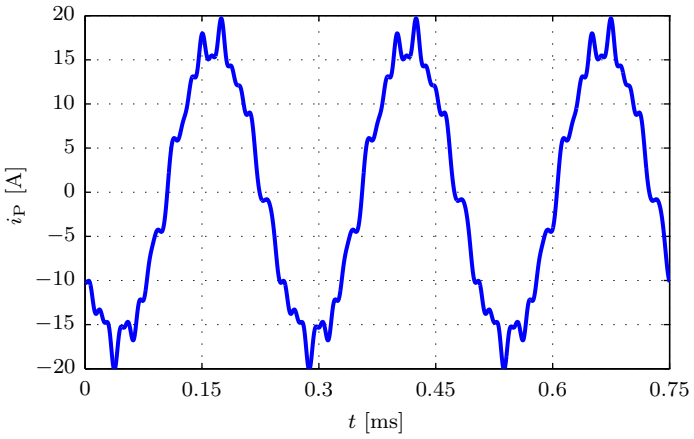

Figure 3. PWM current waveform used for the verification of the model.

Harmonic components present in the waveform shown in Figure 3 are listed in Table 3.

Table 3. Peak values of harmonic components of the current waveform shown in Figure 3.

Frequency	Frequency [kHz]	m	n	Peak Value $\hat{I}_{mn}$ [A]	Sequence
f_0	4	0	1	17	Positive
f_1	32	1	−2	1.27	Positive
f_2	48	1	2	1.1	Negative
f_3	76	2	−1	0.59	Negative
f_4	84	2	1	0.35	Positive

Instantaneous rotor eddy current losses of the benchmark machine shown in Figure 1 are displayed in Figure 4.

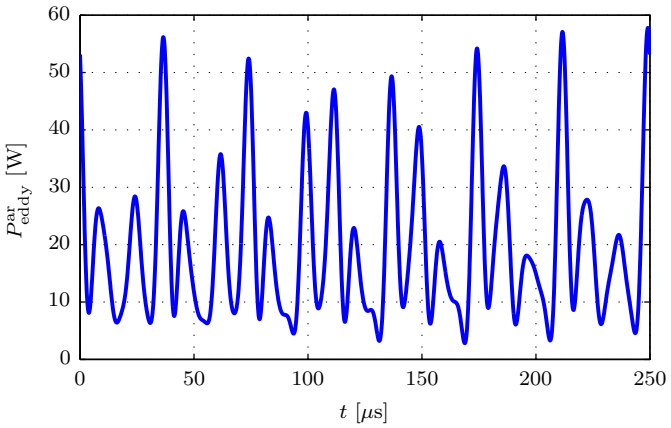

Figure 4. Instantaneous rotor eddy current losses caused by the current waveform shown in Figure 3, obtained by FEM, for the benchmark high-speed machine shown in Figure 1.

These results are obtained by FEM, and time axis in Figure 4 covers 1 fundamental period. By using frequencies and the rotational sequence (positive/negative) given in Table 3, frequencies of harmonic components present in (35) can be determined. They are listed in Table 4. Harmonic components of the waveform shown in Figure 4 are expected to appear at same frequencies.

Table 4. Expected frequencies of rotor eddy current loss components caused by the current harmonic components listed in Table 3.

Frequency	Frequency [kHz]	Frequency	Frequency [kHz]
$f_{01} = f_1 - f_0$	28	$f_{04} = f_4 - f_0$	80
$f_{23} = f_3 - f_2$	28	$f_{14} = f_1 + f_4$	80
$f_{02} = f_0 + f_2$	52	$f_{13} = f_1 + f_3$	108
$f_{14} = f_4 - f_1$	52	$f_{24} = f_2 + f_4$	132
$f_{03} = f_0 + f_3$	80	$f_{34} = f_3 + f_4$	160

After applying fast Fourier transform (FFT) in MATLAB software on the waveform shown in Figure 4, the frequency spectrum shown in Figure 5 is obtained. The actual waveform used for FFT stretches through 5 fundamental periods in order to get accurate spectral analysis.

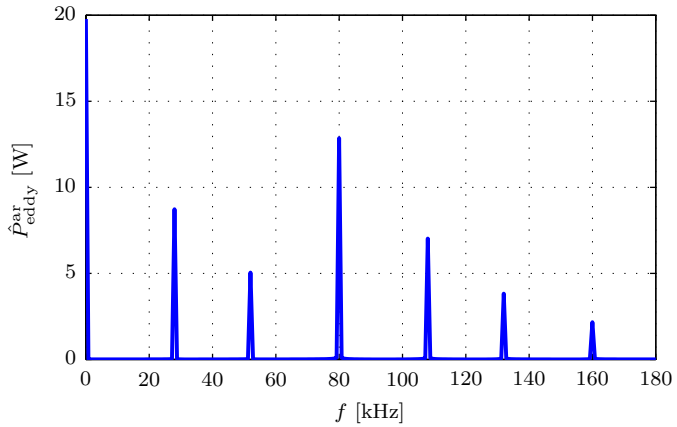

Figure 5. Frequency spectrum of rotor eddy current loss waveform shown in Figure 4.

It can be seen that harmonic components appear exactly at frequencies listed in Table 4, which confirms the validity of the suggested approach. The average value of the waveform shown in Figure 4 is calculated and compared against the result obtained by expression (38). The comparison is shown in Table 5. A good agreement is achieved, with the discrepancy between the HM and FEM of 0.51%.

Table 5. Average value of rotor eddy current losses shown in Figure 4 compared against the result obtained by the HM.

	HM	**FEM**
$P^{\mathrm{ar,av}}_{\mathrm{eddy}}$ [W]	19.9	19.8

The torque of the benchmark machine, which results from the interaction of the PWM current waveform shown in Figure 3 and corresponding rotor eddy currents, is shown in Figure 6. Time scale covers 1 fundamental period, and the result obtained by (39) is shown together with the result obtained by FEM. A good agreement is achieved, with the discrepancy between RMS values obtained by the HM and FEM of 0.84%. PWM harmonics contained in the applied current waveform create rotating waves that move both in the direction of the rotor and in the opposite direction, depending on their spatial order. Field components that rotate in the same direction as the rotor (but at a different speed) pull the rotor forward, creating a positive torque. Components rotating in the opposite direction pull the rotor backward, creating negative torque. Rotating field components of the same spatial order, originating from different PWM harmonics, rotate at different speeds and in both directions. This results in the torque waveform which depends on the instantaneous mutual position of corresponding rotating waves, continuously changing its value between positive and negative.

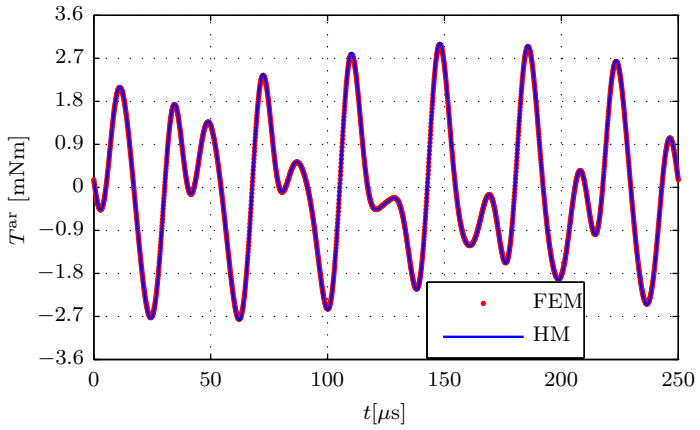

Figure 6. Torque generated by the current waveform shown in Figure 3 and corresponding rotor eddy currents, for the benchmark machine shown in Figure 1.

The torque shown in Figure 6 does not represent the main torque production mechanism in high-speed PM machines and its average value is very small. On the other hand, in high-speed induction machines which have the same geometrical structure as the benchmark machine shown in Figure 1, this is the only torque producing mechanism. In these machines the solid cylinder in the rotor is made of iron, having much higher magnetic permeability than the magnet shown in Figure 1. Furthermore, instead of a retaining sleeve of high-speed PM machines with modest conductivity, the rotors of high-speed induction machines are covered with highly conductive copper coating. Finally, in contrast to PM machines, the traveling wave of the magnetic field created by the fundamental spatial harmonic and the fundamental time harmonic of stator currents moves with respect to the rotor, creating the main component of rotor current. Therefore, in high-speed induction machines the torque shown in Figure 6 is much more significant, and can be accurately and effectively calculated using (39).

According to the author's experience, to achieve satisfactory accuracy by using transient FEM, there should be at least 100 simulation steps per period of each PWM harmonic. This approach is applied for FEM simulations with harmonics listed in Table 3. As the highest considered PWM frequency is 84 kHz, it is required to have at least 2100 simulation steps per fundamental period. To be sure that results are reliable and that transient calculations converged, results from some initial steps have to be discarded. In the work presented here, the complete first fundamental period is omitted for the analysis of the results presented in Figures 4 and 6. As mentioned previously, to get an accurate spectral analysis of the instantaneous rotor loss waveform, the waveform corresponding to 5 fundamental periods is used. The same waveform is used to extract the torque waveform shown in Figure 6. Together with the initial discarded fundamental period, 6 fundamental periods in total have over 12,500 steps, and it takes approximately 2 days to perform this simulation. If only the average rotor losses and the torque waveform are of interest, and not the spectrum of instantaneous rotor losses, reliable FEM results could probably be obtained with 2 or 3 fundamental periods. Therefore, results could be obtained within 1 day. On the other hand, the analytical method is implemented in MATLAB 2019a software, and the computation time is around 2 seconds. The computation time of FEM, of course, depends on the power of used hardware. In this specific case, processor Intel Core i7-3770 CPU (3.40 GHz) is used. FEM computation time also depends on the size of mesh elements. By optimizing the mesh and considering a bigger simulation step to find the compromise between the accuracy and computation time, as well as by using more powerful hardware, FEM computation time might be reduced. However, the difference between the 2 methods is immense, and the finite element model cannot, under any conditions, compete with the presented analytical model in terms of computation time. Furthermore, with a higher switching frequency, the difference between the 2 methods would be even bigger. Namely,

higher frequencies of PWM current harmonics would require both smaller step size and smaller mesh elements in FEM, as the skin depth decreases with the increase of frequency. On the other hand, the value of switching frequency is irrelevant for the computation time of the analytical model.

5. PWM Caused Rotor Eddy Current Losses under Variations of Drive Parameters

As the previously derived analytical method has very low computation time, it can be effectively used for rapid parameter variation studies. To demonstrate the possibilities of the presented method, the influence of switching frequency and retaining sleeve material on rotor eddy current losses is analyzed in this section.

The analysis in terms of the inverter switching frequency is significant for the design of the complete electric drive. If no additional measures (such as soft switching) are applied, the increase of switching frequency increases commutation losses in the inverter, which can significantly influence the overall drive efficiency [23]. Therefore, for high-speed drives, where the fundamental frequency is relatively high, it can be difficult to achieve sufficiently high switching frequency [39]. Consequently, it can be hard to reach values of the frequency modulation ratio m_f used in conventional low-speed drives. In this section, the analysis is done for the range of m_f between 9 and 15 (switching frequency is varied between 36 kHz and 60 kHz).

Properties of the retaining sleeve used until this point correspond to Inconel 718, the material available in the benchmark machine on the available laboratory setup. It is widely used for high-speed PM rotors [40,41]. Likewise, stainless steel and titanium are often used for retaining sleeves of small size high-speed PM machines [42,43]. Therefore, values of the electric conductivity that correspond to these 3 materials are used in this analysis. As losses in the magnet are much smaller than losses in the sleeve, only the influence of the sleeve conductivity on rotor losses is analyzed, while the conductivity of the magnet is kept at the same value as in Table 1.

As a first step, rotor eddy current losses are evaluated under the assumption that only the fundamental current of 12 A RMS flows in stator windings. These losses, indicated as $P_{\text{eddy}}^{\text{ar,fun}}$, and values of the electric conductivity corresponding to 3 considered sleeve materials, are listed in Table 6.

Table 6. Rotor eddy current losses due to the fundamental component of stator current given in Table 3, for the benchmark high-speed PM machine shown in Figure 1, with different retaining sleeve materials, obtained by the HM.

	Inconel 718	**Stainless Steel**	**Titanium**
$P_{\text{eddy}}^{\text{ar,fun}}$ [W]	1.22	2.09	3.34
σ [S/m]	8.33×10^5	14.5×10^5	23.8×10^5

It can be seen that losses increase with the increase of conductivity. As a second step, average rotor eddy current losses are evaluated for current waveforms containing the fundamental component and multiple PWM harmonics. This is done for different values of m_f. Amplitudes of PWM current harmonics are obtained by using values of voltage harmonics given by expression (2) and machine impedance. The impedance is measured by an impedance analyzer at 51 different frequencies between 4 and 165 kHz. Based on these results, analytical expression for the impedance as a function of frequency is obtained by applying the curve fitting procedure. The impedance, of course, increases with the frequency. The rotor (with the relative permeability very close to 1) is removed during the measurement, since otherwise the measured impedance would reflect values corresponding to the blocked rotor test. Amplitudes of PWM current harmonics are obtained by dividing values of voltage harmonics given by (2) with impedance values for target frequencies. Results of average rotor eddy current losses for all 3 considered retaining sleeve materials, for different values of the frequency modulation ratio are shown in Figure 7.

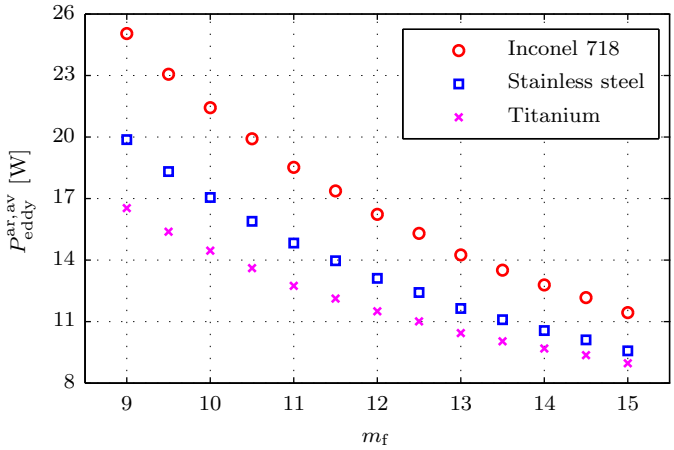

Figure 7. Average rotor eddy current losses for the benchmark high-speed PM machine shown in Figure 1, for different values of m_{f} and different retaining sleeve materials, obtained by the HM.

By looking at Table 6 and Figure 7, it can be seen that electric conductivity of the retaining sleeve has opposite effects on rotor eddy current losses calculated for these 2 situations. This is explained by different mechanisms which dominate eddy current loss behavior for these 2 cases. The fundamental component of stator currents is at relatively low frequency, and eddy currents in the rotor caused by it behave according to so-called resistance limited condition [44], where losses increase with conductivity. More detailed derivation can be found in the first half of Appendix B, where the relation between losses and conductivity is given by expression (A20). On the other hand, PWM harmonics at high frequencies create eddy currents that behave according to so-called inductance limited condition [44], where losses are inversely proportional to the square root of conductivity, as derived in the second part of Appendix B and shown by (A27). As for the benchmark machine, losses caused by PWM harmonics have much higher values than losses caused by the fundamental current, they determine the behavior of overall rotor eddy current losses shown in Figure 7, causing their decrease with the increase of conductivity.

From results presented in Figure 7, it is clear that the increase of switching frequency decreases rotor eddy current losses. Namely, the increase of m_{f} decreases the amplitude of each PWM current harmonic, consequently decreasing the flux density caused by it. However, the increase in m_{f} simultaneously increases the frequency of each current harmonic component. Since higher-order PWM harmonics cause eddy currents in the inductance limited region, losses are proportional to the square of the flux density and the square root of the frequency, as shown by (A27). Therefore, the flux density is a more dominant factor in determining the behavior of eddy current losses, causing them to decrease with the increase of m_{f}.

As a final remark, one could note that losses corresponding to Inconel 718 and $m_{\text{f}} = 10$ in Figure 7 are higher than results shown in Table 5, which correspond to the same value of m_{f}. This is due to the fact that more PWM harmonics than those listed in Table 3 are used to get results shown in Figure 7. As the HM does not suffer from limitations of FEM in terms of computation time, more PWM harmonics can be added without significant additional calculation efforts.

6. Performance Analysis of High-Speed PM Machines at No-Load Conditions

To be able to fully analyze the performance of high-speed PM machines, their behavior at no-load conditions, where there are no stator currents, has to be assessed as well. Similarly to the procedure previously described for the field of stator PWM currents, for

high-speed PM machines with diametrical magnetization, real generic quantities G_1 and G_2 can be defined, with the form equivalent to (6), as

$$G_1(r,\theta_r,t) = \sum_{k_{p1}=-\infty}^{\infty} \hat{\bar{G}}_1(k_{p1}) e^{j\left(k_{p1}\theta_r + l_{p1}(k_{p1})\theta_0 + l_{p1}(k_{p1})\omega_0 t\right)}, \tag{40}$$

and

$$G_2(r,\theta_r,t) = \sum_{k_{p2}=-\infty}^{\infty} \hat{\bar{G}}_2(k_{p2}) e^{j\left(k_{p2}\theta_r + l_{p2}(k_{p2})\theta_0 + l_{p2}(k_{p2})\omega_0 t\right)}. \tag{41}$$

By using (40) and (41), the integral equivalent to (20) can be formed as

$$I^{nl} = \int_{-\pi}^{\pi} G_1 G_2 \mathrm{d}\theta_r = \sum_{k_{p1}=-\infty}^{\infty} \sum_{k_{p2}=-\infty}^{\infty} \hat{\bar{G}}_1(k_{p1}) \hat{\bar{G}}_2(k_{p2}) \cdot \int_{-\pi}^{\pi} e^{j\left((k_{p1}+k_{p2})\theta_r + (l_{p1}(k_{p1})+l_{p2}(k_{p2}))\theta_0 + (l_{p1}(k_{p1})+l_{p2}(k_{p2}))\omega_0 t\right)} \mathrm{d}\theta_r. \tag{42}$$

Integral (42) has a non-zero value only when the following condition is fulfilled

$$k_{p2} = -k_{p1}. \tag{43}$$

When condition (43) is met, as can be seen in Table 2, also the following holds

$$l_{p2}(k_{p2}) = -l_{p1}(k_{p1}), \tag{44}$$

meaning that (42) is always independent of time and simplifies to

$$I^{nl} = 2\pi \sum_{k_p=-\infty}^{\infty} \hat{\bar{G}}_1(k_p) \hat{\bar{G}}_2(-k_p). \tag{45}$$

Quantities G_1 and G_2 for the PM field are real numbers. As they are defined by double sided symmetrical summations, for complex harmonic peak values holds

$$\hat{\bar{G}}_1(-k_p) = \hat{\bar{G}}_1^*(k_p) \quad ; \quad \hat{\bar{G}}_2(-k_p) = \hat{\bar{G}}_2^*(k_p). \tag{46}$$

Therefore, (45) can be rewritten as

$$I^{nl} = 2\pi \sum_{k_p=-\infty}^{\infty} \hat{\bar{G}}_1(k_p) \hat{\bar{G}}_2^*(k_p). \tag{47}$$

By utilizing (46), the following can be written

$$\begin{aligned} \hat{\bar{G}}_1(k_p)\hat{\bar{G}}_2^*(k_p) + \hat{\bar{G}}_1(-k_p)\hat{\bar{G}}_2^*(-k_p) &= \hat{\bar{G}}_1(k_p)\hat{\bar{G}}_2^*(k_p) + \left(\hat{\bar{G}}_1(k_p)\hat{\bar{G}}_2^*(k_p)\right)^* \\ &= 2\Re\left(\hat{\bar{G}}_1(k_p)\hat{\bar{G}}_2^*(k_p)\right), \end{aligned} \tag{48}$$

allowing to rewrite (47) using a single sided summation as

$$I^{nl} = 4\pi \sum_{k_p=1}^{\infty} \Re\left(\hat{\bar{G}}_1(k_p)\hat{\bar{G}}_2^*(k_p)\right). \tag{49}$$

As (49) is time independent, when analyzing only the PM field, the first 2 terms on the right side of (14) vanish. Therefore, no-load rotor eddy current losses (due to interactions between diametrically magnetized rotor magnet and stator slots) can be obtained as

$$P_{\text{eddy}}^{\text{nl}} = 4\pi l_s r_S \sum_{k_p=Y}^{\infty} \Re\left(\hat{\hat{E}}_z(r=r_S,k_p)\hat{\hat{H}}_\theta^*(r=r_S,k_p)\right). \tag{50}$$

Similarly, the no-load torque of high-speed slotted PM machines with diametrical magnetization can be obtained as

$$T^{\text{nl}} = 4\pi l_s r_S^2 \sum_{k_p=1}^{\infty} \Re\left(\hat{\hat{B}}_r(r=r_S,k_p)\hat{\hat{H}}_\theta^*(r=r_S,k_p)\right). \tag{51}$$

All spatial harmonics contribute to the no-load torque given by (51), which is reflected in the fact that lower summation limit is 1. Conversely, the lower summation limit Y in (50) is the lowest value of k_{pm} from (7) higher than 1. As seen by values of l_p given in Table 2, the fundamental harmonic component of the vector potential is constant in the rotor reference frame. Consequently, the corresponding component of the induced electric field is zero, and fundamental component does not contribute to rotor losses.

Rotor eddy current losses at no-load, caused by stator slotting, are evaluated using (50) for the benchmark machine shown in Figure 1, at the rotational speed of 240,000 RPM (corresponding to the fundamental frequency of 4 kHz). Results are compared against those obtained by FEM and shown in Table 7 for the retaining sleeve made of Inconel 718.

Table 7. Rotor eddy current losses at no-load for the benchmark high-speed PM machine shown in Figure 1, with the retaining sleeve made of Inconel 718.

	HM	**FEM**
$P_{\text{eddy}}^{\text{nl}}$ [W]	0.136	0.137

A good agreement between the harmonic model and the finite element model is achieved, with a discrepancy of about 0.73%. Since at the no-load condition stator currents are zero, there is no power transfer from the stator to the rotor. Instead, the power of rotor losses is transferred to the rotor from the mechanical mover. Losses shown in Table 7 are relatively low, but in combination with rotor eddy current losses caused by stator currents, the loss density in the rotor of relatively small volume with limited cooling possibilities can lead to overheating of the magnet. As in Section 5, no-load rotor eddy current losses are also calculated for different retaining sleeve materials. Results are shown in Table 8.

Table 8. Rotor eddy current losses at no-load condition for the benchmark machine shown in Figure 1, with different retaining sleeve materials, obtained by the HM.

	Stainless Steel	**Titanium**
$P_{\text{eddy}}^{\text{nl}}$ [W] (HM)	0.235	0.378

As these losses increase with the increase of conductivity, and they occur at relatively low frequencies, it is evident that rotor eddy currents due to slotting are in the resistance limited region.

Since expression (51) is not dependent on time (and consequently on the position), it can be concluded that high-speed PM machines having rotors with diametrical magnetization do not generate cogging torque. The only torque component at no-load conditions is the breaking torque corresponding to eddy currents in the rotor. The absence of cogging torque can be explained by analyzing the field solution given by (6). As already discussed, each spatial harmonic of the PM field is described by a single traveling wave.

Since the electromagnetic torque can be generated only as a result of the interaction between traveling waves of the same spatial harmonic order, it follows that no-load torque cannot be time-dependent, as there are no multiple traveling waves of the same spatial harmonic order which move one with respect to another and cause variations in the torque. In addition to (51), the no-load torque, corresponding to rotor eddy current losses, can be calculated using the angular speed of the rotor ω_0 as

$$T^{\mathrm{nl}} = -\frac{P^{\mathrm{nl}}_{\mathrm{eddy}}}{\omega_0}, \tag{52}$$

where the torque caused by eddy currents, being a breaking torque, has to be negative. Expression (52) gives the same result as (51).

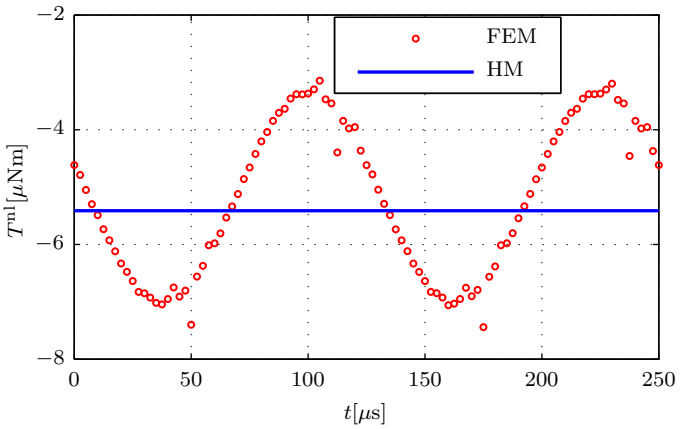

Figure 8. No-load torque for benchmark high-speed PM machine shown in Figure 1.

Figure 8 shows the comparison between the no-load torque obtained by (51) and by finite element model for the benchmark machine shown in Figure 1, within 1 fundamental period. It can be seen that the torque obtained by FEM experiences periodicity at a frequency twice higher than the fundamental frequency of the machine. According to the model derived in this study, which has previously been verified by FEM using flux density and eddy current density waveforms in [29], this should not be the case. Furthermore, it is known that the fundamental frequency of cogging torque for PM machines without skewing is the product of the mechanical frequency (corresponding to the mechanical angular speed) and the least common multiple of the number of slots and the number of poles [45–47]. Therefore, for a machine with 2 poles and an even number of slots, the fundamental frequency of cogging torque is N_{s} times bigger than the fundamental frequency of stator currents, where N_{s} is the number of slots. Consequently, the torque waveform obtained by FEM that is shown in Figure 8 does not represent cogging torque. Having in mind very low values of the no-load torque, which is in the range of μNm, it is most likely that the result obtained by FEM is a consequence of the finite computational precision of the software.

7. Performance Analysis of High-Speed PM Machines at Full Load with PWM Stator Currents

For high-speed PM machines, the electromagnetic field created by both PWM stator currents and rotor magnet determines machine performance. Therefore, to model a high-speed PM machine with diametrical magnetization, models developed from (1) and (6) have to be combined. If both the PM field G^{nl} and the field of PWM currents G^{ar} are present, any generic field quantity G^{ul} can be represented as a combination of individual contributions of these 2 fields

$$G^{\mathrm{ul}}(r, \theta_{\mathrm{r}}, t) = G^{\mathrm{nl}}(r, \theta_{\mathrm{r}}, t) + G^{\mathrm{ar}}(r, \theta_{\mathrm{r}}, t). \tag{53}$$

If the field of stator currents is expressed by its complex representative, as shown in (19), and 2 different field quantities G_1 and G_2 are considered, it can be written

$$G_1^{\mathrm{ul}} = G_1^{\mathrm{nl}} + \frac{1}{2}(\bar{G}_1^{\mathrm{ar}} + \bar{G}_1^{\mathrm{ar}*}) \quad ; \quad G_2^{\mathrm{ul}} = G_2^{\mathrm{nl}} + \frac{1}{2}(\bar{G}_2^{\mathrm{ar}} + \bar{G}_2^{\mathrm{ar}*}). \tag{54}$$

If the integral equivalent to (20) and (42) is formed using (54), it can be written

$$\begin{aligned} I^{\mathrm{ul}} &= \int_{-\pi}^{\pi} G_1^{\mathrm{ul}} G_2^{\mathrm{ul}} \mathrm{d}\theta_{\mathrm{r}} = \int_{-\pi}^{\pi} G_1^{\mathrm{nl}} G_2^{\mathrm{nl}} \mathrm{d}\theta_{\mathrm{r}} + \frac{1}{4}\int_{-\pi}^{\pi} (\bar{G}_1^{\mathrm{ar}} + \bar{G}_1^{\mathrm{ar}*})(\bar{G}_2^{\mathrm{ar}} + \bar{G}_2^{\mathrm{ar}*})\mathrm{d}\theta_{\mathrm{r}} \\ &+ \frac{1}{2}\int_{-\pi}^{\pi} G_1^{\mathrm{nl}}(\bar{G}_2^{\mathrm{ar}} + \bar{G}_2^{\mathrm{ar}*})\mathrm{d}\theta_{\mathrm{r}} + \frac{1}{2}\int_{-\pi}^{\pi} G_2^{\mathrm{nl}}(\bar{G}_1^{\mathrm{ar}} + \bar{G}_1^{\mathrm{ar}*})\mathrm{d}\theta_{\mathrm{r}} = I_1^{\mathrm{ul}} + I_2^{\mathrm{ul}} + I_3^{\mathrm{ul}} + I_4^{\mathrm{ul}}. \end{aligned} \tag{55}$$

Integral I_1^{ul} from (55) is actually the no-load integral I^{nl} given by (42), which results in expression (49). Integral I_2^{ul} corresponds to the integral I^{ar} given by (20) and eventually results in (35). Integrals I_3^{ul} and I_4^{ul} in (55) model the interaction between the PM field and the field of stator PWM currents and they are analyzed further on.

As any quantity derived from the no-load field is a real number, corresponding terms for the same absolute value of k_{p} are conjugated with respect to one another. This allows to express generic no-load quantity G^{nl} using a single-sided summation, as

$$\begin{aligned} G^{\mathrm{nl}}(r,\theta_{\mathrm{r}},t) &= \sum_{k_{\mathrm{p}}=1}^{\infty} \Big(\hat{\bar{G}}^{\mathrm{nl}}(r,k_{\mathrm{p}}) e^{j\left(k_{\mathrm{p}}\theta_{\mathrm{r}} + l_{\mathrm{p}}(k_{\mathrm{p}})\theta_0 + l_{\mathrm{p}}(k_{\mathrm{p}})\omega_0 t\right)} \\ &+ \hat{\bar{G}}^{\mathrm{nl}*}(r,k_{\mathrm{p}}) e^{-j\left(k_{\mathrm{p}}\theta_{\mathrm{r}} + l_{\mathrm{p}}(k_{\mathrm{p}})\theta_0 + l_{\mathrm{p}}(k_{\mathrm{p}})\omega_0 t\right)} \Big) = \bar{G}^{\mathrm{nl}}(r,\theta_{\mathrm{r}},t) + \bar{G}^{\mathrm{nl}*}(r,\theta_{\mathrm{r}},t), \end{aligned} \tag{56}$$

where $\hat{\bar{G}}^{\mathrm{nl}}$ is the complex harmonic peak value of the complex generic no-load field quantity $\bar{G}^{\mathrm{nl}}$. If (56) is inserted into integrals I_3^{ul} and I_4^{ul} given in (55), it can be written

$$I_3^{\mathrm{ul}} + I_4^{\mathrm{ul}} = \frac{1}{2}\int_{-\pi}^{\pi} \left(\bar{G}_1^{\mathrm{nl}} + \bar{G}_1^{\mathrm{nl}*}\right)(\bar{G}_2^{\mathrm{ar}} + \bar{G}_2^{\mathrm{ar}*})\mathrm{d}\theta_{\mathrm{r}} + \frac{1}{2}\int_{-\pi}^{\pi} \left(\bar{G}_2^{\mathrm{nl}} + \bar{G}_2^{\mathrm{nl}*}\right)(\bar{G}_1^{\mathrm{ar}} + \bar{G}_1^{\mathrm{ar}*})\mathrm{d}\theta_{\mathrm{r}}. \tag{57}$$

Both integrals in (57) have the same form as the integral in (21). Therefore, (57) can be rewritten as

$$\begin{aligned} I_3^{\mathrm{ul}} + I_4^{\mathrm{ul}} &= \int_{-\pi}^{\pi} \Re\left(\bar{G}_1^{\mathrm{nl}}\bar{G}_2^{\mathrm{ar}}\right)\mathrm{d}\theta_{\mathrm{r}} + \int_{-\pi}^{\pi} \Re\left(\bar{G}_1^{\mathrm{nl}}\bar{G}_2^{\mathrm{ar}*}\right)\mathrm{d}\theta_{\mathrm{r}} \\ &+ \int_{-\pi}^{\pi} \Re\left(\bar{G}_2^{\mathrm{nl}}\bar{G}_1^{\mathrm{ar}}\right)\mathrm{d}\theta_{\mathrm{r}} + \int_{-\pi}^{\pi} \Re\left(\bar{G}_2^{\mathrm{nl}}\bar{G}_1^{\mathrm{ar}*}\right)\mathrm{d}\theta_{\mathrm{r}} = I_3^{\mathrm{ul,a}} + I_3^{\mathrm{ul,b}} + I_4^{\mathrm{ul,a}} + I_4^{\mathrm{ul,b}}. \end{aligned} \tag{58}$$

Both $\bar{G}_1^{\mathrm{nl}}$ and $\bar{G}_2^{\mathrm{nl}}$ have the form of the first term in (56), while $\bar{G}_1^{\mathrm{ar}}$ and $\bar{G}_2^{\mathrm{ar}}$ have the form given by (1). Therefore, if a single PWM harmonic is considered, it can be written

$$\begin{aligned} I_3^{\mathrm{ul,a}} + I_4^{\mathrm{ul,a}} = \sum_{k_{\mathrm{p}}=1}^{\infty} \sum_{L=-\infty}^{\infty} \int_{-\pi}^{\pi} \Re\Big(&\left(\hat{\bar{G}}_1^{\mathrm{nl}}(k_{\mathrm{p}})\hat{\bar{G}}_2^{\mathrm{ar}}(L,m,n) + \hat{\bar{G}}_2^{\mathrm{nl}}(k_{\mathrm{p}})\hat{\bar{G}}_1^{\mathrm{ar}}(L,m,n)\right) \\ &\cdot e^{j\left((k_{\mathrm{p}}+3L-n)\theta_{\mathrm{r}} + (l_{\mathrm{p}}(k_{\mathrm{p}})+3L-n)\theta_0 + \left(l_{\mathrm{p}}(k_{\mathrm{p}})+m\cdot m_{\mathrm{f}}+3L\right)\omega_0 t\right)} \Big)\mathrm{d}\theta_{\mathrm{r}}. \end{aligned} \tag{59}$$

The previous expression has a non-zero value only when the following holds

$$3L - n = -k_{\mathrm{p}}, \tag{60}$$

transforming the term which is multiplied by θ_0 in the exponent into

$$l_{\mathrm{p}}(k_{\mathrm{p}}) + 3L - n = l_{\mathrm{p}}(k_{\mathrm{p}}) - k_{\mathrm{p}} = \pm 1, \tag{61}$$

and allowing to express the angular frequency from (59) as

$$\big(l_{\mathrm{p}}(k_{\mathrm{p}}) + m \cdot m_{\mathrm{f}} + 3L\big)\omega_0 = \big(m \cdot m_{\mathrm{f}} + n + l_{\mathrm{p}}(k_{\mathrm{p}}) - k_{\mathrm{p}}\big)\omega_0 = (m \cdot m_{\mathrm{f}} + n \pm 1)\omega_0. \tag{62}$$

Last steps in (61) and (62) result from the relation between l_{p} and k_{p} shown in Table 2. By expressing L using (60) and accounting for (61) and (62), (59) can be rewritten as

$$I_3^{\mathrm{ul,a}} + I_4^{\mathrm{ul,a}} = 2\pi \sum_{k_{\mathrm{p}}=1}^{\infty} \Re\Bigg(\Bigg(\hat{\bar{G}}_1^{\mathrm{nl}}(k_{\mathrm{p}}) \hat{\bar{G}}_2^{\mathrm{ar}}\Big(L = \frac{n - k_{\mathrm{p}}}{3}, m, n\Big) + \hat{\bar{G}}_2^{\mathrm{nl}}(k_{\mathrm{p}}) \hat{\bar{G}}_1^{\mathrm{ar}}\Big(L = \frac{n - k_{\mathrm{p}}}{3}, m, n\Big) \Bigg) e^{j(\pm\theta_0 + (m \cdot m_{\mathrm{f}} + n \pm 1)\omega_0 t)} \Bigg). \tag{63}$$

As k_{p} in (63) takes only positive values, by observing Table 2 it can be concluded that (61) takes value 1 for the PM field spatial harmonics of following orders

$$k_{\mathrm{p}} = pN_{\mathrm{s}} - 1, \; p \in \mathbb{N}. \tag{64}$$

On the other hand, (61) takes value -1 for the fundamental spatial harmonic of the PM field and spatial harmonics of following orders

$$k_{\mathrm{p}} = pN_{\mathrm{s}} + 1, \; p \in \mathbb{N}. \tag{65}$$

By inserting (64) and (65) into (63), if k_{p} is expressed through p, it can be written

$$\begin{aligned} I_3^{\mathrm{ul,a}} + I_4^{\mathrm{ul,a}} = {} & 2\pi \sum_{p=1}^{\infty} \Re\Bigg(\Bigg(\hat{\bar{G}}_1^{\mathrm{nl}}(k_{\mathrm{p}} = pN_{\mathrm{s}} - 1) \hat{\bar{G}}_2^{\mathrm{ar}}\Big(L = \frac{n - pN_{\mathrm{s}} + 1}{3}, m, n\Big) \\ & + \hat{\bar{G}}_2^{\mathrm{nl}}(k_{\mathrm{p}} = pN_{\mathrm{s}} - 1) \hat{\bar{G}}_1^{\mathrm{ar}}\Big(L = \frac{n - pN_{\mathrm{s}} + 1}{3}, m, n\Big) \Bigg) e^{j((mm_{\mathrm{f}} + n + 1)\omega_0 t + \theta_0)} \Bigg) \\ & + 2\pi \sum_{p=0}^{\infty} \Re\Bigg(\Bigg(\hat{\bar{G}}_1^{\mathrm{nl}}(k_{\mathrm{p}} = pN_{\mathrm{s}} + 1) \hat{\bar{G}}_2^{\mathrm{ar}}\Big(L = \frac{n - pN_{\mathrm{s}} - 1}{3}, m, n\Big) \\ & + \hat{\bar{G}}_2^{\mathrm{nl}}(k_{\mathrm{p}} = pN_{\mathrm{s}} + 1) \hat{\bar{G}}_1^{\mathrm{ar}}\Big(L = \frac{n - pN_{\mathrm{s}} - 1}{3}, m, n\Big) \Bigg) e^{j((mm_{\mathrm{f}} + n - 1)\omega_0 t - \theta_0)} \Bigg). \end{aligned} \tag{66}$$

As L is an integer, and the number of slots N_{s} for a 3-phase machine is divisible by 3, the first 2 terms in (66) exist only for harmonics of negative sequence, for n given by (5), while the last 2 terms exist only for harmonics of positive sequence, for n given by (4).

Similarly to (59), for the second part of (58) it can be written

$$\begin{aligned} I_3^{\mathrm{ul,b}} + I_4^{\mathrm{ul,b}} = \sum_{k_{\mathrm{p}}=1}^{\infty} \sum_{L=-\infty}^{\infty} \int_{-\pi}^{\pi} \Re\Bigg(\Big(\hat{\bar{G}}_1^{\mathrm{nl}}(k_{\mathrm{p}}) \hat{\bar{G}}_2^{\mathrm{ar}*}(L, m, n) + \hat{\bar{G}}_2^{\mathrm{nl}}(k_{\mathrm{p}}) \hat{\bar{G}}_1^{\mathrm{ar}*}(L, m, n) \Big) \\ \cdot e^{j\left((k_{\mathrm{p}} - 3L + n)\theta_{\mathrm{r}} + (l_{\mathrm{p}}(k_{\mathrm{p}}) - 3L + n)\theta_0 + \left(l_{\mathrm{p}}(k_{\mathrm{p}}) - m \cdot m_{\mathrm{f}} - 3L\right)\omega_0 t\right)} \Bigg) \mathrm{d}\theta_{\mathrm{r}}. \end{aligned} \tag{67}$$

The previous expression has a non-zero value only when the following holds

$$3L - n = k_\mathrm{p}, \tag{68}$$

transforming the term which is multiplied by θ_0 into

$$l_\mathrm{p}(k_\mathrm{p}) - 3L + n = l_\mathrm{p}(k_\mathrm{p}) - k_\mathrm{p} = \pm 1, \tag{69}$$

and allowing to express the angular frequency from (67) as

$$\left(l_\mathrm{p}(k_\mathrm{p}) - m \cdot m_\mathrm{f} - 3L\right)\omega_0 = \left(l_\mathrm{p}(k_\mathrm{p}) - k_\mathrm{p} - m \cdot m_\mathrm{f} - n\right)\omega_0 = (\pm 1 - (m \cdot m_\mathrm{f} + n))\omega_0. \tag{70}$$

By expressing L using (68) and taking into account (69) and (70), (67) can be rewritten as

$$I_3^{\mathrm{ul,b}} + I_4^{\mathrm{ul,b}} = 2\pi \sum_{k_\mathrm{p}=1}^{\infty} \Re\Bigg(\Bigg(\hat{\bar{G}}_1^{\mathrm{nl}}(k_\mathrm{p}) \hat{\bar{G}}_2^{\mathrm{ar}*}\left(L = \frac{n + k_\mathrm{p}}{3}, m, n\right) + \hat{\bar{G}}_2^{\mathrm{nl}}(k_\mathrm{p}) \hat{\bar{G}}_1^{\mathrm{ar}*}\left(L = \frac{n + k_\mathrm{p}}{3}, m, n\right) \Bigg) \cdot e^{j(\pm\theta_0 + (\pm 1 - (m \cdot m_\mathrm{f} + n))\omega_0 t)} \Bigg). \tag{71}$$

By taking into account the relation between l_p and k_p given in Table 2, for positive values of k_p, and by inserting (64) and (65) into (71), it can be written

$$\begin{aligned} I_3^{\mathrm{ul,b}} + I_4^{\mathrm{ul,b}} = {} & 2\pi \sum_{p=1}^{\infty} \Re\Bigg(\Bigg(\hat{\bar{G}}_1^{\mathrm{nl}}(k_\mathrm{p} = pN_\mathrm{s} - 1) \hat{\bar{G}}_2^{\mathrm{ar}*}\left(L = \frac{n + pN_\mathrm{s} - 1}{3}, m, n\right) \\ & + \hat{\bar{G}}_2^{\mathrm{nl}}(k_\mathrm{p} = pN_\mathrm{s} - 1) \hat{\bar{G}}_1^{\mathrm{ar}*}\left(L = \frac{n + pN_\mathrm{s} - 1}{3}, m, n\right) \Bigg) e^{j((1 - m \cdot m_\mathrm{f} - n)\omega_0 t + \theta_0)} \Bigg) \\ & + 2\pi \sum_{p=0}^{\infty} \Re\Bigg(\Bigg(\hat{\bar{G}}_1^{\mathrm{nl}}(k_\mathrm{p} = pN_\mathrm{s} + 1) \hat{\bar{G}}_2^{\mathrm{ar}*}\left(L = \frac{n + pN_\mathrm{s} + 1}{3}, m, n\right) \\ & + \hat{\bar{G}}_2^{\mathrm{nl}}(k_\mathrm{p} = pN_\mathrm{s} + 1) \hat{\bar{G}}_1^{\mathrm{ar}*}\left(L = \frac{n + pN_\mathrm{s} + 1}{3}, m, n\right) \Bigg) e^{-j((m \cdot m_\mathrm{f} + n + 1)\omega_0 t + \theta_0)} \Bigg). \end{aligned} \tag{72}$$

Again, by having in mind that L is an integer and N_s is divisible by 3, the first 2 terms in (72) exist only for the PWM harmonics of positive sequence, for n given by (4), while the last 2 terms exist only for PWM harmonics of negative sequence, for n given by (5).

By inserting (66) and (72) into (58), the final form of the generic integral for the calculation of the electromagnetic torque and rotor eddy current losses due to the interaction between the permanent magnet field and stator field are obtained. By looking at terms containing the frequency in these expressions it can be concluded that the average torque and the average rotor eddy current losses are created only by the armature currents at the fundamental frequency, for which holds

$$m \cdot m_\mathrm{f} + n = \pm 1. \tag{73}$$

Higher-order PWM harmonics of stator currents cause sinusoidal variations of the torque and rotor eddy current losses when interacting with the PM field. Namely, they create rotating field harmonic components that experience a relative movement with respect to the harmonic components of the same spatial order created by the PM field. Since the interaction of the corresponding PM and stator field components is dependent on their mutual position, time dependency appears in the result of this interaction.

By substituting G_1 with B_r and G_2 with H_θ in (66) and (72), for both the PM (superscript "nl") and stator (superscript "ar") fields, if all PWM harmonics are included, the torque which is the result of the interaction between the PM and stator field can be ex-

pressed as the combination of torques generated by all positive sequence PWM harmonics ($T^{\mathrm{nl,ar}}_{n+}$) and all negative sequence PWM harmonics ($T^{\mathrm{nl,ar}}_{n-}$), as

$$
\begin{aligned}
T^{\mathrm{nl,ar}}(t) &= l_{\mathrm{s}} r_S^2 \sum_{\substack{m=0\\ m>0}}^{\infty} \sum_{n=-\infty}^{\infty} \left(I_3^{\mathrm{ul,a}} + I_4^{\mathrm{ul,a}} + I_3^{\mathrm{ul,b}} + I_4^{\mathrm{ul,b}} \right) = T^{\mathrm{nl,ar}}_{n+}(t) + T^{\mathrm{nl,ar}}_{n-}(t) \\
&= 2\pi l_s r_S^2 \sum_{p=0}^{\infty} \sum_{m=0}^{\infty} \sum_{n_{\mathrm{p}}} \Re \Bigg(\Bigg(\hat{\hat{B}}^{\mathrm{nl}}_{rg}(r = r_S, k_{\mathrm{p}} = pN_{\mathrm{s}} + 1) \\
&\qquad \cdot \hat{H}^{\mathrm{ar}}_{\theta g}\left(r = r_S, L = \frac{n_{\mathrm{p}} - pN_{\mathrm{s}} - 1}{3}, m, n_{\mathrm{p}} \right) \\
&\quad + \hat{H}^{\mathrm{nl}}_{\theta g}(r = r_S, k_{\mathrm{p}} = pN_{\mathrm{s}} + 1) \hat{\hat{B}}^{\mathrm{ar}}_{rg}\left(r = r_S, L = \frac{n_{\mathrm{p}} - pN_{\mathrm{s}} - 1}{3}, m, n_{\mathrm{p}} \right) \Bigg) \\
&\quad \cdot e^{j\left((m \cdot m_{\mathrm{f}} + n_{\mathrm{p}} - 1)\omega_0 t - \theta_0 \right)} \Bigg) \\
&\quad + 2\pi l_s r_S^2 \sum_{p=1}^{\infty} \sum_{m=0}^{\infty} \sum_{n_{\mathrm{p}}} \Re \Bigg(\Bigg(\hat{\hat{B}}^{\mathrm{nl}}_{rg}(r = r_S, k_{\mathrm{p}} = pN_{\mathrm{s}} - 1) \\
&\qquad \cdot \hat{H}^{\mathrm{ar*}}_{\theta g}\left(r = r_S, L = \frac{n_{\mathrm{p}} + pN_{\mathrm{s}} - 1}{3}, m, n_{\mathrm{p}} \right) \\
&\quad + \hat{H}^{\mathrm{nl}}_{\theta g}(r = r_S, k_{\mathrm{p}} = pN_{\mathrm{s}} - 1) \hat{\hat{B}}^{\mathrm{ar*}}_{rg}\left(r = r_S, L = \frac{n_{\mathrm{p}} + pN_{\mathrm{s}} - 1}{3}, m, n_{\mathrm{p}} \right) \Bigg) \\
&\quad \cdot e^{j\left((1 - m \cdot m_{\mathrm{f}} - n_{\mathrm{p}})\omega_0 t + \theta_0 \right)} \Bigg) \\
&\quad + 2\pi l_s r_S^2 \sum_{p=1}^{\infty} \sum_{m=0}^{\infty} \sum_{n_{\mathrm{n}}} \Re \Bigg(\Bigg(\hat{\hat{B}}^{\mathrm{nl}}_{rg}(r = r_S, k_{\mathrm{p}} = pN_{\mathrm{s}} - 1) \\
&\qquad \cdot \hat{H}^{\mathrm{ar}}_{\theta g}\left(r = r_S, L = \frac{n_{\mathrm{n}} - pN_{\mathrm{s}} + 1}{3}, m, n_{\mathrm{n}} \right) \\
&\quad + \hat{H}^{\mathrm{nl}}_{\theta g}(r = r_S, k_{\mathrm{p}} = pN_{\mathrm{s}} - 1) \hat{\hat{B}}^{\mathrm{ar}}_{rg}\left(r = r_S, L = \frac{n_{\mathrm{n}} - pN_{\mathrm{s}} + 1}{3}, m, n_{\mathrm{n}} \right) \Bigg) \\
&\quad \cdot e^{j\left((m \cdot m_{\mathrm{f}} + n_{\mathrm{n}} + 1)\omega_0 t + \theta_0 \right)} \Bigg) \\
&\quad + 2\pi l_s r_S^2 \sum_{p=0}^{\infty} \sum_{m=0}^{\infty} \sum_{n_{\mathrm{n}}} \Re \Bigg(\Bigg(\hat{\hat{B}}^{\mathrm{nl}}_{rg}(r = r_S, k_{\mathrm{p}} = pN_{\mathrm{s}} + 1) \\
&\qquad \cdot \hat{H}^{\mathrm{ar*}}_{\theta g}\left(r = r_S, L = \frac{n_{\mathrm{n}} + pN_{\mathrm{s}} + 1}{3}, m, n_{\mathrm{n}} \right) \\
&\quad + \hat{H}^{\mathrm{nl}}_{\theta g}(r = r_S, k_{\mathrm{p}} = pN_{\mathrm{s}} + 1) \hat{\hat{B}}^{\mathrm{ar*}}_{rg}\left(r = r_S, L = \frac{n_{\mathrm{n}} + pN_{\mathrm{s}} + 1}{3}, m, n_{\mathrm{n}} \right) \Bigg) \\
&\quad \cdot e^{-j\left((m \cdot m_{\mathrm{f}} + n_{\mathrm{n}} + 1)\omega_0 t + \theta_0 \right)} \Bigg),
\end{aligned}
\tag{74}
$$

where n_{p} and n_{n} represent values of n giving positive and negative sequence currents, respectively. The total torque of a high-speed PM machine fed by PWM currents is obtained by adding up the no-load torque given by (51), the torque created by the interaction between stator currents and rotor eddy currents caused by them—expression (39), and the torque created by the interaction between the PM field and the field of stator currents given by (74)

$$
T(t) = T^{\mathrm{nl}} + T^{\mathrm{ar}}(t) + T^{\mathrm{nl,ar}}(t). \tag{75}
$$

The instantaneous torque obtained by (75) of the benchmark machine is shown in Figure 9, for the PWM current waveform shown in Figure 3. The initial rotor positions is chosen to correspond to the generator mode with $i_{\mathrm{d}} = 0$ control, providing the maximum torque for a given current.

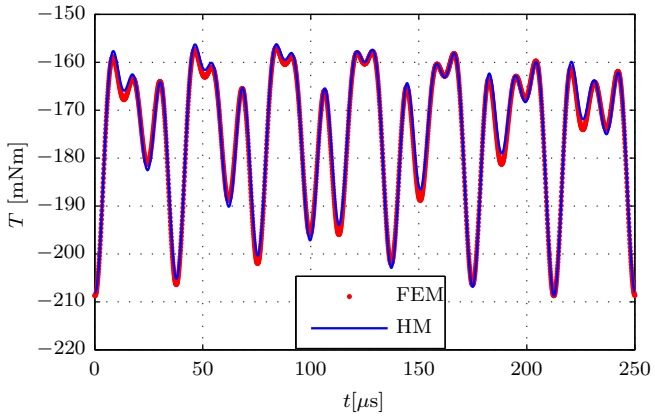

Figure 9. Instantaneous torque of the benchmark machine shown in Figure 1, for the PWM current waveform shown in Figure 3.

The torque waveform is compared against the result obtained by the finite element model. A good agreement is achieved between torque values obtained by the HM and FEM, with the RMS discrepancy of 0.25%.

Mathematically, the condition under which PWM current harmonic contributes to the average rotor eddy current losses in a high-speed PM machine with diametrical magnetization is given by (73). Physically, in the reference frame of the rotor, each spatial harmonic created by this current harmonic rotates in the same direction and at the same speed as the corresponding spatial harmonic generated due to interactions between the permanent magnet and stator slots. For higher-order PWM harmonics that do not satisfy (73), the resultant eddy current density in the rotor changes with time, causing sinusoidal variations of eddy current losses. This is displayed in Figure 10, where a hypothetical fifth spatial harmonic is used for the illustration, and all waveforms are shown in the reference frame fixed to the current density waveform created by the PM field (J_z^{nl}). If the current density waveform caused by the armature field (J_z^{ar}) moves with respect to J_z^{nl}, the peak value of the resultant current density changes with time.

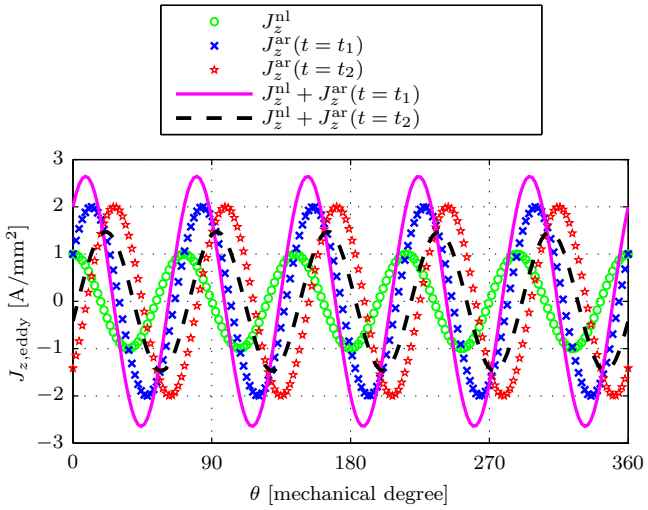

Figure 10. Superposition of eddy current density in the rotor caused by the PM field (J_z^{nl}) and stator field of a higher order PWM harmonic (J_z^{ar}), for 2 different instants of time t_1 and t_2.

PWM harmonics which satisfy (73) could theoretically be created by sideband harmonics for which holds $m > 0$. However, with realistic values of frequency modulation ratio m_f this would mean that negative n with high absolute value corresponds to these harmonics. Since amplitudes of voltage harmonics are determined by Bessel functions of the first kind of order n, as shown in (2), peak values of these voltage harmonics would be very low. Consequently, their effects can be neglected and in practice only the combination $m = 0$ and $n = 1$ result in zero values of (62) and (70). Therefore, only the last 2 terms in (66) and first 2 terms in (72) are considered, as they represent positive sequence of PWM stator currents. By substituting $m = 0$ and $n = 1$ in these expressions, the generic integral (58) simplifies to

$$\begin{aligned} I_3^{\mathrm{ul}} + I_4^{\mathrm{ul}} = 2\pi \sum_{p=0}^{\infty} \Re\Bigg(& \hat{\hat{G}}_1^{\mathrm{nl}}(k_{\mathrm{p}} = pN_{\mathrm{s}} + 1)\hat{\hat{G}}_2^{\mathrm{ar,fun}}\left(L = -\frac{pN_{\mathrm{s}}}{3}\right)e^{-j\theta_0} \\ & + \hat{\hat{G}}_2^{\mathrm{nl}}(k_{\mathrm{p}} = pN_{\mathrm{s}} + 1)\hat{\hat{G}}_1^{\mathrm{ar,fun}}\left(L = -\frac{pN_{\mathrm{s}}}{3}\right)e^{-j\theta_0}\Bigg) \\ + 2\pi \sum_{p=1}^{\infty} \Re\Bigg(& \hat{\hat{G}}_1^{\mathrm{nl}}(k_{\mathrm{p}} = pN_{\mathrm{s}} - 1)\hat{\hat{G}}_2^{\mathrm{ar,fun}*}\left(L = \frac{pN_{\mathrm{s}}}{3}\right)e^{j\theta_0} \\ & + \hat{\hat{G}}_2^{\mathrm{nl}}(k_{\mathrm{p}} = pN_{\mathrm{s}} - 1)\hat{\hat{G}}_1^{\mathrm{ar,fun}*}\left(L = \frac{pN_{\mathrm{s}}}{3}\right)e^{j\theta_0}\Bigg), \end{aligned} \tag{76}$$

where "fun" in superscripts of stator field quantities indicates the fundamental component of stator currents. Since the surface integral in the Poynting's theorem contains the product $E_z H_\theta$, for the calculation of average rotor eddy current losses, generic field quantities G_1 and G_2 are replaced by E_z and H_θ, respectively. The fundamental spatial harmonics of both the PM field and of the field of the fundamental component of stator currents move at the same speed as the rotor. Consequently, the fundamental spatial component of the induced electric field in the rotor reference frame is zero for both field components and first 2 terms in (76) are zero for $p = 0$. Therefore, the contribution to the average rotor eddy current losses due to the interaction between the PM and the stator field can be expressed, by using a single summation, as

$$\begin{aligned} P_{\mathrm{eddy}}^{\mathrm{nl,ar,av}} = 2\pi l_{\mathrm{s}} r_S \sum_{p=1}^{\infty} \Re\Bigg(& \hat{\hat{E}}_z^{\mathrm{nl}}(r = r_S, k_{\mathrm{p}} = pN_{\mathrm{s}} + 1)\hat{\hat{H}}_\theta^{\mathrm{ar,fun}}\left(r = r_S, L = -\frac{pN_{\mathrm{s}}}{3}\right)e^{-j\theta_0} \\ & + \hat{\hat{H}}_\theta^{\mathrm{nl}}(r = r_S, k_{\mathrm{p}} = pN_{\mathrm{s}} + 1)\hat{\hat{E}}_z^{\mathrm{ar,fun}}\left(r = r_S, L = -\frac{pN_{\mathrm{s}}}{3}\right)e^{-j\theta_0} \\ & + \hat{\hat{E}}_z^{\mathrm{nl}}(r = r_S, k_{\mathrm{p}} = pN_{\mathrm{s}} - 1)\hat{\hat{H}}_\theta^{\mathrm{ar,fun}*}\left(r = r_S, L = \frac{pN_{\mathrm{s}}}{3}\right)e^{j\theta_0} \\ & + \hat{\hat{H}}_\theta^{\mathrm{nl}}(r = r_S, k_{\mathrm{p}} = pN_{\mathrm{s}} - 1)\hat{\hat{E}}_z^{\mathrm{ar,fun}*}\left(r = r_S, L = \frac{pN_{\mathrm{s}}}{3}\right)e^{j\theta_0}\Bigg). \end{aligned} \tag{77}$$

Total average rotor eddy current losses of a high-speed PM machine under PWM supply ($P_{\mathrm{eddy}}^{\mathrm{nl,ar,av}}$) are obtained by adding contributions of the PM field—expression (50), of the armature field—expression (38), and by their combination—expression (77).

$$P_{\mathrm{eddy}}^{\mathrm{av}} = P_{\mathrm{eddy}}^{\mathrm{nl}} + P_{\mathrm{eddy}}^{\mathrm{ar,av}} + P_{\mathrm{eddy}}^{\mathrm{nl,ar,av}}. \tag{78}$$

Since $P_{\mathrm{eddy}}^{\mathrm{nl,ar,av}}$ exists only when both the PM field and the stator field are present in the machine, the result of (77) has to be validated together with other 2 terms present in (78). To verify losses obtained by (77), a finite element model of the benchmark machine is used, where the retaining sleeve is made of Inconel 718. Stator windings are supplied only with the fundamental component of PWM currents given in Table 3. Results are shown in

Figure 11 for different values of the initial rotor position θ_0, together with results obtained by (78) for the retaining sleeve made of titanium and stainless steel. A good agreement is achieved between the HM and FEM, with the discrepancy between RMS values obtained by the HM and FEM of 2.5 %. Since both the PM field and the fundamental component of stator currents cause eddy current losses in the resistance limited region, total losses increase with the increase of conductivity.

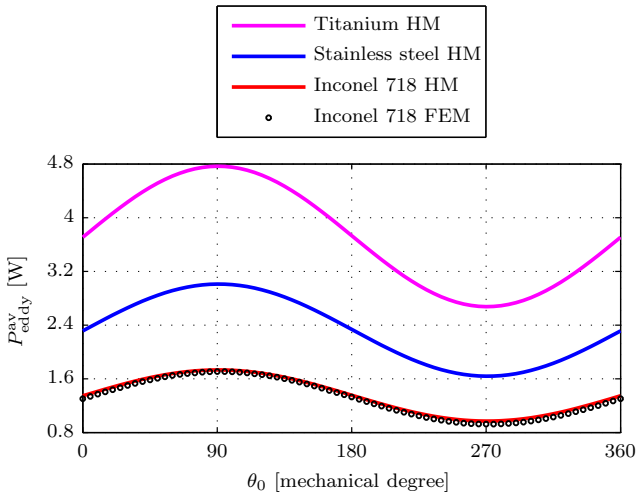

Figure 11. Rotor eddy current losses for the benchmark machine shown in Figure 1, caused by the PM and the fundamental component of the stator current waveform given in Table 3, for different retaining sleeve materials, as a function of the rotor initial position.

The initial rotor positions of 0 and 180 degrees in Figure 11 correspond to the motor and generator mode with $i_{\text{d}} = 0$ control, respectively. This control strategy is often used in high-performance high-speed drives [48]. Since the PM and the stator field are orthogonal in this case, there is no contribution of (77) and rotor eddy current losses can be obtained solely by adding up individual contributions of the PM field and the armature field. For $i_{\text{d}} \neq 0$, the contribution of (77) has to be included to get total losses. Positions where θ_0 takes values of 90 and 270 degrees in Figure 11 correspond to the full alignment of the PM field and the stator field and their full opposition, respectively. When 2 fields are fully aligned, the resultant magnetic field is of the highest intensity, giving the maximum value of the rotor eddy current losses. Contrary to this, when 2 fields are opposing one another, the resultant field is of the lowest intensity, giving minimal rotor eddy current losses. However, these 2 initial positions have no practical relevance in the machine operation, as they result in zero average electromagnetic torque.

8. On the Experimental Verification of Electromagnetic Torque and Rotor Eddy Current Losses in High-Speed Machines Supplied by PWM Inverters

Measurement of electromagnetic torque and rotor eddy current losses presents a significant challenge for high-speed machines supplied by PWM inverters. In contrast to conventional low-speed machines, a torque sensor can not be easily used on the rotating shaft of a high-speed machine, as it can influence rotor dynamics and cause serious mechanical issues [49]. Therefore, torque is usually measured without mechanical connection to the rotating rotor, or with the locked rotor. The former could be done by using eddy-current brake [49], or by measuring the reaction torque of the stator [50]. To capture torque waveforms caused by PWM, the torque sensor would need to have very high bandwidth, since the instantaneous torque contains components at high frequencies, as shown in this study. This also holds for the torque under locked rotor conditions. Consequently, torque measurement would require a specially designed high-performance setup which is not available to the author. Therefore, it is not possible to support the electromagnetic torque calculation presented in this paper with experimental data.

Eddy current losses can be experimentally obtained through the thermometric method, by measuring the change in the rotor temperature [51,52]. As this requires the installation of temperature sensors on the rotor, it is practically impossible to perform it with the rotating high-speed rotor. Consequently, rotor eddy current losses caused by the PM field cannot be measured in this way, as they appear only when the rotor magnet moves with respect to stator slots. Alternatively, these losses could be extracted from total losses measured in a given test, as they always exist together with other loss components. However, rotor losses are often relatively small in comparison to other losses which appear simultaneously, such as mechanical, iron, or copper losses. Therefore, a high measurement error appears while applying the loss segregation method, as a small relative error in the estimation of total losses (or other loss components) represents a large error for rotor losses [53]. Having in mind low values of PM-caused rotor eddy current losses calculated in this study, and significantly higher values of other loss components in the setup available to the author, it is not realistic to expect that measurement of PM-caused rotor eddy current losses by the loss segregation method would give any reliable result.

Finally, rotor losses caused by stator currents can be measured, and this was done previously by the author and presented in [31]. The measurement was performed without the rotation, with the goal to reduce the number of involved loss components and to minimize measurement error. Stator windings were powered with identical currents in 2 tests: with the locked rotor and with the rotor removed from the stator bore. In this way, only the electrical power at stator terminals is measured, and rotor losses are obtained as a difference between the values measured in 2 tests. This measurement, however, could not be done with a real PWM waveform, as it was not possible to keep the same values of PWM current harmonics in both tests. Namely, the inverter imposes PWM voltage harmonics. High-frequency rotor eddy currents strongly affect the field in the machine when the rotor is present, which influences the inductance and for the same voltage harmonics results in different PWM currents in comparison to the test without the rotor, as shown in [31]. Therefore, the test was done by supplying the machine with sinusoidal currents at different frequencies, where the current at each frequency was maintained at the same value in both tests. These sinusoidal currents resemble individual PWM harmonics. Rotor losses obtained with each individual harmonic were added up, and in this way losses calculated by (38) were indirectly measured. To be able to mimic PWM current harmonics with reasonable amplitudes corresponding to m_f between 9 and 16, the emulated PWM harmonics corresponded to a somewhat lower fundamental frequency of 1.5 kHz. The measurement was simultaneously performed on 2 identical benchmark machines with the topology shown in Figure 1. Results obtained in [31] are displayed in Figure 12, and they confirm the validity of the suggested analytical approach.

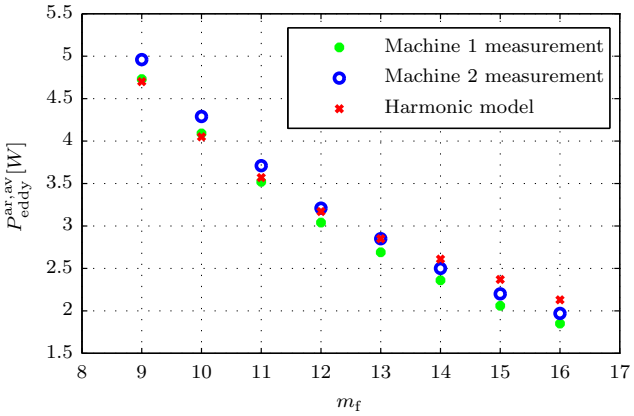

Figure 12. Measured and predicted rotor eddy current losses of the benchmark machine shown in Figure 1. Adapted with permission from ref. [31]. Copyright 2015 IEEE.

9. Conclusions

The work presented in this study has demonstrated a thorough procedure for the analytical modeling of high-speed permanent magnet and induction machines supplied by pulse-width modulated inverters. The focus of the presented analysis has been put on the effective calculation of rotor eddy current losses and electromagnetic torque, as main performance indicators for these machines. The analysis has been split into several parts, where the effects of the permanent magnet and PWM currents are first assessed individually, and eventually, their combined effects have been studied.

Based on the results of the work presented in this paper, it is possible to get a clear insight into the performance of high-speed machines. Harmonic components in the frequency spectrum of instantaneous rotor eddy current losses have been identified and related to the rotational sequence of different harmonics in stator currents. Furthermore, it has been mathematically shown that high-speed permanent magnet machines with diametrical magnetization do not generate cogging torque due to the specific magnetic field distribution in the air gap, determined by the magnetization pattern on the rotor.

All the findings presented in this study have been verified with a finite element model, which confirmed the validity of the used approach. Furthermore, it has been demonstrated that the presented approach is superior in comparison to the finite element method in terms of computation time when considering pulse width modulated supply. As high-speed electrical machines are inherently driven by power electronics converters, the method presented in this work offers a very useful and reliable alternative to FEM for the analysis of high-speed drives.

By utilizing models developed in this study, it is possible to accurately and quickly perform design optimization of high-speed electric machines. As the presented approach uses an analytical and mesh-free method, fast parameter variations can be done during the machine design stage. Geometrical parameters, material properties, and different inverter parameters (such as switching frequency) can be varied, as has been demonstrated. Consequently, their effect on losses, total electromagnetic torque, and torque ripple can be evaluated, without occupying significant computational resources.

Funding: This research received no external funding.

Institutional Review Board Statement: Not applicable.

Informed Consent Statement: Not applicable.

Data Availability Statement: Not applicable.

Conflicts of Interest: The author declares no conflict of interest.

Abbreviations

The following abbreviations are used in this manuscript:

RPM	revolutions per minute
PM	permanent magnet
PWM	pulse-width modulated
MEC	magnetic equivalent circuits
VSI	voltage source inverter
2D	two-dimensional
HM	harmonic modeling
FEM	finite element model
FFT	fast Fourier transform
RMS	root mean square

Appendix A. Poynting's Theorem

In a system with eddy current density $\vec{J}_{\text{eddy}}$ and externally imposed current density $\vec{J}_{\text{i}}$, the total current density can be defined using the electric conductivity σ and the induced electric field $\vec{E}$ as

$$\vec{J} = \vec{J}_{\text{eddy}} + \vec{J}_{\text{i}} = \sigma\vec{E} + \vec{J}_{\text{i}}. \tag{A1}$$

If (A1) is inserted into Ampère's law, it can be written

$$\nabla \times \vec{H} = \sigma\vec{E} + \vec{J}_{\text{i}}. \tag{A2}$$

If (A2) is combined with Faraday's law

$$\nabla \times \vec{E} = -\frac{\partial \vec{B}}{\partial t}, \tag{A3}$$

by performing the dot product of (A2) with $\vec{E}$ and the dot product of (A3) with $\vec{H}$, it can be written

$$\vec{E} \cdot \left(\nabla \times \vec{H}\right) = \sigma|\vec{E}|^2 + \vec{E} \cdot \vec{J}_{\text{i}} \;\; ; \;\; \vec{H} \cdot \left(\nabla \times \vec{E}\right) = -\vec{H} \cdot \frac{\partial \vec{B}}{\partial t}, \tag{A4}$$

where $|\vec{E}|$ is the intensity of the electric field vector $\vec{E}$. By applying the following vector calculus identity [34]

$$\nabla \cdot \left(\vec{E} \times \vec{H}\right) = \vec{H} \cdot \left(\nabla \times \vec{E}\right) - \vec{E} \cdot \left(\nabla \times \vec{H}\right), \tag{A5}$$

expressions given by (A4) can be merged into

$$\nabla \cdot \left(\vec{E} \times \vec{H}\right) = -\vec{H} \cdot \frac{\partial \vec{B}}{\partial t} - \sigma|\vec{E}|^2 - \vec{E} \cdot \vec{J}_{\text{i}}. \tag{A6}$$

By exploiting the constitutive equation of a permanent magnet with the remanent flux density $\vec{B}_{\text{rem}}$

$$\vec{B} = \mu_0\mu_{\text{r}}\vec{H} + \vec{B}_{\text{rem}}, \tag{A7}$$

expression (A6) can be rewritten as

$$\nabla \cdot \left(\vec{E} \times \vec{H}\right) = -\mu_0\mu_{\text{r}}\vec{H} \cdot \frac{\partial \vec{H}}{\partial t} - \vec{H} \cdot \frac{\partial \vec{B}_{\text{rem}}}{\partial t} - \sigma|\vec{E}|^2 - \vec{E} \cdot \vec{J}_{\text{i}}. \tag{A8}$$

The first term on the right side of (A8) can be transformed in the following way

$$\vec{H} \cdot \frac{\partial \vec{H}}{\partial t} = \frac{1}{2}\left(\frac{\partial \vec{H}}{\partial t} \cdot \vec{H} + \vec{H} \cdot \frac{\partial \vec{H}}{\partial t}\right) = \frac{1}{2}\frac{\partial}{\partial t}\left(\vec{H} \cdot \vec{H}\right) = \frac{1}{2}\frac{\partial}{\partial t}|\vec{H}|^2, \tag{A9}$$

where $|\vec{H}|$ is the intensity of the magnetic field strength vector $\vec{H}$. After inserting (A9) into (A8), it can be written

$$-\nabla \cdot \left(\vec{E} \times \vec{H}\right) = \frac{\mu_0\mu_{\text{r}}}{2}\frac{\partial}{\partial t}|\vec{H}|^2 + \vec{H} \cdot \frac{\partial \vec{B}_{\text{rem}}}{\partial t} + \sigma|\vec{E}|^2 + \vec{E} \cdot \vec{J}_{\text{i}}. \tag{A10}$$

By applying a volume integral on both sides of (A10) and assuming that the volume V does not change with time, it can be written

$$-\int_V \nabla \cdot \left(\vec{E} \times \vec{H}\right) \mathrm{d}V = \frac{\mu_0}{2} \frac{\partial}{\partial t} \int_V \mu_\mathrm{r} |\vec{H}|^2 \mathrm{d}V + \int_V \vec{H} \cdot \frac{\partial \vec{B}_\mathrm{rem}}{\partial t} \mathrm{d}V + \int_V \sigma |\vec{E}|^2 \mathrm{d}V + \int_V \vec{E} \cdot \vec{J}_\mathrm{i} \mathrm{d}V. \tag{A11}$$

If the divergence theorem [34] is applied to the left side of (A11), it transforms into a surface integral, giving the final form of Poynting's theorem

$$-\oint_S \left(\vec{E} \times \vec{H}\right) \cdot \vec{n} \mathrm{d}S = \frac{\mu_0}{2} \frac{\partial}{\partial t} \int_V \mu_\mathrm{r} |\vec{H}|^2 \mathrm{d}V + \int_V \vec{H} \cdot \frac{\partial \vec{B}_\mathrm{rem}}{\partial t} \mathrm{d}V + \int_V \sigma |\vec{E}|^2 \mathrm{d}V + \int_V \vec{E} \cdot \vec{J}_\mathrm{i} \mathrm{d}V, \tag{A12}$$

where S is a closed surface surrounding volume V and $\vec{n}$ is the outward normal on surface S.

Appendix B. Resistance and Inductance Limited Eddy Current Losses

The power of eddy current losses P_eddy, as of any other Joule losses described in terms of the circuit theory, can be expressed as

$$P_\mathrm{eddy} = R_\mathrm{eddy} I_\mathrm{eddy}^2, \tag{A13}$$

where R_eddy is the resistance of the path where eddy currents flow, and I_eddy is the RMS value of the eddy current intensity. Relation (A13) can be expressed by the RMS value of the electromotive force which causes eddy currents E_eddy, eddy currents' angular frequency ω_eddy, and the inductance of the path in which eddy currents flow L_eddy

$$P_\mathrm{eddy} = R_\mathrm{eddy} \frac{E_\mathrm{eddy}^2}{R_\mathrm{eddy}^2 + \omega_\mathrm{eddy}^2 L_\mathrm{eddy}^2}. \tag{A14}$$

The electromotive force is the result of time variations of the magnetic flux density B_eddy which in the reference frame of the conducting material varies at the angular frequency ω_eddy. If constant k_e, specific to the individual machine, is introduced, the RMS value of the induced electromotive force can be represented as

$$E_\mathrm{eddy} = k_e l_\mathrm{s} \omega_\mathrm{eddy} B_\mathrm{eddy}, \tag{A15}$$

where l_s is the active length of the machine. Then, (A14) can be rewritten as

$$P_\mathrm{eddy} = R_\mathrm{eddy} \frac{k_e^2 l_\mathrm{s}^2 \omega_\mathrm{eddy}^2 B_\mathrm{eddy}^2}{R_\mathrm{eddy}^2 + \omega_\mathrm{eddy}^2 L_\mathrm{eddy}^2}. \tag{A16}$$

When eddy currents are governed by the resistance limited condition, at relatively low values of frequency ω_eddy, the following relation holds

$$R_\mathrm{eddy} >> \omega_\mathrm{eddy} L_\mathrm{eddy}. \tag{A17}$$

The second term in the denominator of (A16) can be omitted, simplifying it to

$$P^R_{\text{eddy}} = \frac{k_e^2 l_s^2 \omega^2_{\text{eddy}} B^2_{\text{eddy}}}{R^R_{\text{eddy}}}, \tag{A18}$$

where R^R_{eddy} stands for the resistance of the path in which eddy currents flow under resistance limited conditions. Resistance limited eddy currents create the magnetic field orthogonal to the magnetic field that causes them. Therefore, the current density does not redistribute throughout the depth of the conducting material, since there is no interaction between the original magnetic field and the reaction field of eddy currents. Consequently, the cross sectional area over which eddy currents flow remains unaffected. Then R^R_{eddy} can be expressed, using constant k_ρ, as

$$R^R_{\text{eddy}} = \frac{k_\rho l_s}{\sigma}, \tag{A19}$$

where σ is the electric conductivity. By inserting (A19) into (A18), the power of eddy current losses under resistance limited conditions can be expressed as

$$P^R_{\text{eddy}} = \frac{k_e^2}{k_\rho} l_s B^2_{\text{eddy}} \sigma \omega^2_{\text{eddy}} = k_R l_s B^2_{\text{eddy}} \sigma \omega^2_{\text{eddy}}, \tag{A20}$$

where k_R is the constant determined by the construction of the machine. As can be seen, eddy current losses under resistance limited conditions are linearly dependent on conductivity of the considered region and proportional to the square of the frequency.

When eddy currents are governed by the inductance limited condition, at high values of frequency ω_{eddy}, the following relation holds

$$R_{\text{eddy}} << \omega_{\text{eddy}} L_{\text{eddy}}. \tag{A21}$$

The first term in the denominator of (A16) can be omitted, simplifying (A16) to

$$P^L_{\text{eddy}} = \frac{R^L_{\text{eddy}}}{L^2_{\text{eddy}}} k_e^2 l_s^2 B^2_{\text{eddy}}, \tag{A22}$$

where R^L_{eddy} is the resistance of the path in which eddy currents flow under inductance limited conditions.

Inductance limited eddy currents create the magnetic field which is in counter phase with the magnetic field that causes them. Due to this, the resultant magnetic field does not fully penetrate the conducting material. Consequently, the cross sectional area in which eddy currents flow is proportional to the skin depth, making R^L_{eddy} inversely proportional to it. By taking into account the definition of the skin depth δ

$$\delta = \sqrt{\frac{2}{\omega_{\text{eddy}} \mu \sigma}}, \tag{A23}$$

where μ is the permeability of the conducting region, R^L_{eddy} can be expressed as

$$R^L_{\text{eddy}} = \frac{k_r l_s}{\sigma \delta} = k_\delta l_s \sqrt{\frac{\omega_{\text{eddy}}}{\sigma}}, \tag{A24}$$

where k_r and k_δ are constants. If (A24) is inserted into (A22), it can be written

$$P^L_{\text{eddy}} = \frac{k_e^2 k_\delta l_s^3}{L^2_{\text{eddy}}} B^2_{\text{eddy}} \sqrt{\frac{\omega_{\text{eddy}}}{\sigma}}. \tag{A25}$$

If inductance L_{eddy} is expressed using the inductance per the unit of length l_{eddy}

$$L_{\text{eddy}} = l_{\text{eddy}} \cdot l_{\text{s}}, \tag{A26}$$

Equation (A25) can be rewritten as

$$P_{\text{eddy}}^{L} = \frac{k_e^2 k_\delta}{l_{\text{eddy}}^2} l_{\text{s}} B_{\text{eddy}}^2 \sqrt{\frac{\omega_{\text{eddy}}}{\sigma}} = k_L l_{\text{s}} B_{\text{eddy}}^2 \sqrt{\frac{\omega_{\text{eddy}}}{\sigma}}, \tag{A27}$$

where k_L is the constant determined by the design of the machine. As can be seen, eddy current losses under inductance limited conditions are inversely proportional to the square root of the electric conductivity of the considered region, and directly proportional to the square root of the frequency.

References

1. Lee, D.-K.; Ro, J.-S. Analysis and Design of a High-Performance Traction Motor for Heavy-Duty Vehicles. *Energies* **2020**, *13*, 3150. [CrossRef]
2. Bhagubai, P.P.C.; Sarrico, J.G.; Fernandes, J.F.P.; Costa Branco, P.J. Design, Multi-Objective Optimization, and Prototyping of a 20 kW 8000 rpm Permanent Magnet Synchronous Motor for a Competition Electric Vehicle. *Energies* **2020**, *13*, 2465. [CrossRef]
3. Lehmann, R.; Petuchow, A.; Moullion, M.; Künzler, M.; Windel, C.; Gauterin, F. Fluid Choice Based on Thermal Model and Performance Testing for Direct Cooled Electric Drive. *Energies* **2020**, *13*, 5867. [CrossRef]
4. Acquaviva, A.; Skoog, S.; Grunditz, E.; Thiringer, T. Electromagnetic and Calorimetric Validation of a Direct Oil Cooled Tooth Coil Winding PM Machine for Traction Application. *Energies* **2020**, *13*, 3339. [CrossRef]
5. Popa, D.-C.; Jurca, N.-F.; Inte, R.A.; Hrusch, N.; Hemphill, J.; Cantemir, C.G. Zero-Airgap Induction Motor Used to Drive a Transmission Oil Pump. *Energies* **2020**, *13*, 4286. [CrossRef]
6. Pop-Pîgleşan, F.; Pop, A.-C.; Marțiş, C. Synchronous Reluctance Machines for Automotive Cooling Fan Systems: Numerical and Experimental Study of Different Slot-Pole Combinations and Winding Types. *Energies* **2021**, *14*, 460. [CrossRef]
7. Noguchi, T.; Kano, M. Development of 150,000 r/min, 1.5 kW Permanent-Magnet Motor for Automotive Supercharger. In Proceedings of the 2007 7th International Conference on Power Electronics and Drive Systems, Bangkok, Thailand, 27–30 November 2007; pp. 183–188.
8. Hong, D; Lee, T.; Jeong, Y. Design and Experimental Validation of a High-Speed Electric Turbocharger Motor Considering Variation of the $\boldsymbol{L/D}$ Ratio. *IEEE Trans. Magn.* **2018**, *54*, 1–4. [CrossRef]
9. Gerada, D.; Mebarki, A.; Brown, N.L.; Gerada, C.; Cavagnino, A.; Boglietti, A. High-Speed Electrical Machines: Technologies, Trends, and Developments. *IEEE Trans. Ind. Electron.* **2014**, *61*, 2946–2959. [CrossRef]
10. Shen, J.-X.; Qin, X.-F. Investigation of Rotor Eddy Current Loss in High-Speed PM Synchronous Motor with Various PWM Strategies. In Proceedings of the 2020 Fifteenth International Conference on Ecological Vehicles and Renewable Energies (EVER), Monte-Carlo, Monaco, 10–12 September 2020; pp. 1–5. [CrossRef]
11. Yamazaki, K.; Watari, S. Loss analysis of permanent-magnet motor considering carrier harmonics of PWM inverter using combination of 2-D and 3-D finite-element method. *IEEE Trans. Magn.* **2005**, *41*, 1980–1983. [CrossRef]
12. Yamazaki, K.; Abe, A. Loss Investigation of Interior Permanent-Magnet Motors Considering Carrier Harmonics and Magnet Eddy Currents. *IEEE Trans. Ind. Appl.* **2009**, *45*, 659–665. [CrossRef]
13. Tang, Y. Multi-Excited Reluctance Machines. Ph.D. Thesis, Eindhoven University of Technology, Eindhoven, The Netherlands, 2017.
14. Bao, J. Hybrid Modeling Technique for Nonlnear 2D Electromagnetic Problems. Ph.D. Thesis, Eindhoven University of Technology, Eindhoven, The Netherlands, 2017.
15. Tariq, A.R.; Nino-Baron, C.E.; Strangas, E.G. Iron and Magnet Losses and Torque Calculation of Interior Permanent Magnet Synchronous Machines Using Magnetic Equivalent Circuit. *IEEE Trans. Magn.* **2010**, *46*, 4073–4080. [CrossRef]
16. Hemeida, A.; Sergeant, P. Analytical modeling of eddy current losses in Axial Flux PMSM using resistance network. In Proceedings of 2014 International Conference on Electrical Machines (ICEM), Berlin, Germany, 2–5 September 2014; pp. 2688–2694. [CrossRef]
17. Jumayev, S.; Borisavljevic, A.; Boynov, K.; Lomonova, E.A.; Pyrhonen, J. Analysis of rotor eddy current losses in slotless high-speed permanent magnet machines. In Proceedings of the 2014 16th European Conference on Power Electronics and Applications, Lappeenranta, Finland, 26–28 August 2014; pp. 1–10. [CrossRef]
18. Jumayev, S.; Boynov, K.O.; Paulides, J.J.H.; Lomonova, E.A.; Pyrhonen, J. Slotless PM Machines with Skewed Winding Shapes: 3-D Electromagnetic Semianalytical Model. *IEEE Trans. Magn.* **2016**, *52*, 1–12. [CrossRef]
19. Deng, F.; Nehl, T.W. Analytical modeling of eddy-current losses caused by pulse-width-modulation switching in permanent-magnet brushless direct-current motors. *IEEE Trans. Magn.* **1998**, *34*, 3728–3736. [CrossRef]
20. Markovic, M.; Perriard, Y. Analytical Solution for Rotor Eddy-Current Losses in a Slotless Permanent-Magnet Motor: The Case of Current Sheet Excitation. *IEEE Trans. Magn.* **2008**, *44*, 386–393. [CrossRef]

21. Pfister, P.; Yin, X.; Fang, Y. Slotted Permanent-Magnet Machines: General Analytical Model of Magnetic Fields, Torque, Eddy Currents, and Permanent-Magnet Power Losses Including the Diffusion Effect. *IEEE Trans. Magn.* **2016**, *52*, 1–13. [CrossRef]
22. Hannon, B.; Sergeant, P.; Dupre, L. Time-and Spatial-Harmonic Content in Synchronous Electrical Machines. *IEEE Trans. Magn.* **2017**, *53*, 1–11. [CrossRef]
23. Schwager, L.; Tuysuz, A.; Zwyssig, C.; Kolar, J.W. Modeling and Comparison of Machine and Converter Losses for PWM and PAM in High-Speed Drives. *IEEE Trans. Ind. Appl.* **2014**, *50*, 995–1006. [CrossRef]
24. Holm, S.R. Modelling and Optimization of a Permanent Magnet Machine in a Flywheel. Ph.D. Thesis, Delft University of Technology, Delft, The Netherlands, 2003.
25. Holmes, D.G.; Lipo, T.A. *Pulse Width Modulation for Power Converters, Principles and Practice*; John Wiley and Sons, Inc.: Hoboken, NJ, USA, 2003; ISBN 0-471-20814-0.
26. Wang, X.; Sala, G.; Zhang, H.; Gu, C.; Buticchi, G.; Formentini, A.; Gerada, C.; Wheeler, P. Torque Ripple Reduction in Sectored Multi Three-Phase Machines Based on PWM Carrier Phase Shift. *IEEE Trans. Ind. Electron.* **2020**, *67*, 4315–4325. [CrossRef]
27. Wang, X.; Yan, H.; Sala, G.; Buticchi, G.; Gu, C.; Zhao, W.; Xu, L.; Zhang, H. Selective Torque Harmonic Elimination for Dual Three-Phase PMSM Based on PWM Carrier Phase Shift. *IEEE Trans. Power Electron.* **2020**, *35*, 13255–13269. [CrossRef]
28. Merdzan, M.; Borisavljevic, A.; Lomonova, E.A. Modeling the Influence of Commutation in Voltage Source Inverters on Rotor Losses of Permanent Magnet Machines. In Proceedings of the 2014 16th European Conference on Power Electronics and Applications, Lappeenranta, Finland, 26–28 August 2014; pp. 1–10.
29. Merdzan, M. Computationally Efficient Semi-Analytical Model for the Calculation of the No-Load Magnetic Field in High-Speed Permanent Magnet Machines. In Proceedings of the 2020 Fifteenth International Conference on Ecological Vehicles and Renewable Energies (EVER), Monte-Carlo, Monaco, 10–12 September 2020; pp. 1–7.
30. Hannon, B.; Sergeant, P.; Dupre, L. Study of the Effect of a Shielding Cylinder on the Torque in a Permanent-Magnet Synchronous Machine Considering Two Torque-Producing Mechanisms. *IEEE Trans. Magn.* **2017**, *53*, 1–8. [CrossRef]
31. Merdzan, M.; Paulides, J.J.H.; Borisavljevic, A.; Lomonova, E.A. The influence of the inverter switching frequency on rotor losses in high-speed permanent magnet machines: An experimental study. In Proceedings of the 2015 IEEE International Electric Machines and Drives Conference (IEMDC), Coeur d'Alene, ID, USA, 10–13 May 2015; pp. 1628–1633. [CrossRef]
32. Huppunen, J. High-Speed Solid-Rotor Induction Machine Electromagnetic Calculation and Design. Ph.D. Thesis, Lappeenranta University of Technology, Lappeenranta, Finland, 2004.
33. Lahteenmaki, J. Design and Voltage Supply of High-Speed Induction Machines. Ph.D. Thesis, Helsinki University of Technology, Helsinki, Finland, 2002.
34. Furlani, E.P. *Permanent Magnet and Electromechanical Devices*; Academic Press: Cambridge, MA, USA, 2001; ISBN 0-12-269951-3.
35. Hannon, B. Fourier-Based Modeling of Permanent-Magnet Synchronous Machines Operating at High Speed. Ph.D. Thesis, Ghent University, Ghent, Belgium, 2017.
36. Jumayev, S. High-Speed Slotless Permanent Magnet Machines. Ph.D. Thesis, Eindhoven University of Technology, Eindhoven, The Netherlands, 2017.
37. Sprangers, R.L.J. Towards Increased Understanding of Low-Power Induction and Synchronous Reluctance Machines. Ph.D. Thesis, Eindhoven University of Technology, Eindhoven, The Netherlands, 2015.
38. Borisavljevic, A. Limits, Modeling and Design of High-Speed Permanent Magnet Machines. Ph.D. Thesis, Delft University of Technology, Delft, The Netherlands, 2011.
39. Stumpf P.; Halasz, S. Optimization of PWM for the Overmodulation Region of Two-Level Inverters. *IEEE Trans. Ind. Appl.* **2018**, *54*, 3393–3404. [CrossRef]
40. Uzhegov, N. Design and Material Selection of High-Speed Rotating Electrical Machines. Ph.D. Thesis, Lappeenranta University of Technology, Lappeenranta, Finland, 2016.
41. Kolondzovski, Z. Thermal and Mechanical Analyses of High-Speed Permanent- Magnet Electrical Machines. Ph.D. Thesis, Aalto University, Espoo, Finland, 2010.
42. Li, W.; Qiu, H.; Zhang, X.; Cao, J.; Yi, R. Analyses on Electromagnetic and Temperature Fields of Superhigh-Speed Permanent-Magnet Generator With Different Sleeve Materials. *IEEE Trans. Ind. Electron.* **2014**, *61*, 3056–3063. [CrossRef]
43. Zwyssig C.; Round, S.D.; Kolar, J.W. An Ultrahigh-Speed, Low Power Electrical Drive System. *IEEE Trans. Ind. Electron.* **2008**, *55*, 577–585. [CrossRef]
44. Hendershot, J.R.; Miller, T.J. *Design of Brushless Permanent-Magnet Machines*; Motor Design Books LLC: Venice, FL, USA, 2010; ISBN 978-0-9840687-0-8.
45. Dosiek L.; Pillay, P. Cogging Torque Reduction in Permanent Magnet Machines. *IEEE Trans. Ind. Appl.* **2007**, *43*, 1565–1571. [CrossRef]
46. Wanjiku, J.; Khan, M.A.; Barendse, P.S.; Pillay, P. Influence of Slot Openings and Tooth Profile on Cogging Torque in Axial-Flux PM Machines. *IEEE Trans. Ind. Electron.* **2015**, *62*, 7578–7589. [CrossRef]
47. Hanselman, D. *Brushless Permanent Magnet Motor Design*; Magna Physics Publishing: Madison, WI, USA, 2006; ISBN 1-881855-15-5.
48. Borisavljevic, A.; Brands, M.; Lomonova, E. Vector Control of Very-High-Speed PM Machines. In Proceedings of the 2012 XX International Conference on Electrical Machines, Marseille, France, 2–5 September 2012; pp. 2462–2468.
49. Pfister P.; Perriard, Y. Torque measurement methods for very high speed synchronous motors. In Proceedings of the 2008 18th International Conference on Electrical Machines, Vilamoura, Portugal, 6–9 September 2008; pp. 1–5. [CrossRef]

50. Zwyssig, C.; Round, S.D.; Kolar, J.W. Analytical and Experimental Investigation of a Low Torque, Ultra-High Speed Drive System. In Proceedings of the 2006 IEEE Industry Applications Conference Forty-First IAS Annual Meeting, Tampa, FL, USA, 8–12 October 2006; pp. 1507–1513. [CrossRef]
51. Yamazaki, K.; Shina, M.; Miwa, M.; Hagiwara, J. Investigation of Eddy Current Loss in Divided Nd–Fe–B Sintered Magnets for Synchronous Motors Due to Insulation Resistance and Frequency. *IEEE Trans. Magn.* **2008**, *44*, 4269–4272. [CrossRef]
52. Aoyama, Y.; Miyata K.; Ohashi, K. Simulations and experiments on eddy current in Nd-Fe-B magnet. *IEEE Trans. Magn.* **2005**, *41*, 3790–3792. [CrossRef]
53. Xiao, C.; Chen, G.; Odendaal, W.G.H. Overview of Power Loss Measurement Techniques in Power Electronics Systems. *IEEE Trans. Ind. Appl.* **2007**, *43*, 657–664. [CrossRef]